

TOPICAL REVIEW

Fast micromagnetic simulations on GPU—recent advances made with mumax³

To cite this article: J Leliaert *et al* 2018 *J. Phys. D: Appl. Phys.* **51** 123002

View the [article online](#) for updates and enhancements.



LIVE WEBINAR

NanoRaman: Correlated Tip-Enhanced Optical Spectroscopy and Scanning Probe Microscopy

Thursday 8 March 15.00 GMT

REGISTER NOW!

physicsworld.com

Topical Review

Fast micromagnetic simulations on GPU—recent advances made with mumax³

J Leliaert¹, M Dvornik², J Mulkers^{1,3}, J De Clercq¹, M V Milošević³
and B Van Waeyenberge¹

¹ Department of Solid State Sciences, Ghent University, Ghent, Belgium

² University of Gothenburg, Gothenburg, Sweden

³ Department of Physics, Antwerp University, Antwerp, Belgium

E-mail: bartel.vanwaeyenberge@ugent.be

Received 23 January 2017, revised 2 December 2017

Accepted for publication 26 January 2018

Published 21 February 2018



CrossMark

Abstract

In the last twenty years, numerical modeling has become an indispensable part of magnetism research. It has become a standard tool for both the exploration of new systems and for the interpretation of experimental data. In the last five years, the capabilities of micromagnetic modeling have dramatically increased due to the deployment of graphical processing units (GPU), which have sped up calculations to a factor of 200. This has enabled many studies which were previously unfeasible. In this topical review, we give an overview of this modeling approach and show how it has contributed to the forefront of current magnetism research.

Keywords: magnetism, micromagnetic simulation, GPU

(Some figures may appear in colour only in the online journal)

1. Introduction to micromagnetism

1.1. Historical overview of micromagnetism

Micromagnetism is the theory which describes magnetization on the intermediate scales above those where individual atomic spins have to be taken into account, but below the macroscopic scale on which entire domains are observed [1]. So, micromagnetism is a continuum theory of magnetic materials at the picosecond timescale and nanometer to micrometer length scale. The first step towards this theory was taken by Weiss in 1907 [2], by investigating why some magnetic materials do not display net magnetization: he conjectured that a ferromagnetic material could contain several uniformly magnetized domains, in which the magnetization points in different directions. Furthermore, knowing that the magneto-static field is not strong enough to explain the alignment of the magnetic moments within these domains [3], he attributed this to an unknown field which he called the Weiss molecular field, which later was shown to result from the quantum-mechanical Heisenberg–Dirac exchange interaction [4].

In 1919, Barkhausen observed that when a magnet is brought in the vicinity of another magnetic material, the magnetization of the latter changes in discrete jumps, leading to Barkhausen noise [5], which he attributed to switching of the individual domains. Barkhausen associated and explained his observations with domain theory, already twelve years before domains were first visualized by Bitter [6]. However, his explanation was not entirely correct: while investigating the reversal of magnetic wires [7], Sixtus and Tonks concluded that the domains themselves do not switch direction, but the domain boundaries move and thus enlarge the domains with an energetically favorable magnetization direction.

Bloch was the first to investigate domain walls theoretically [8] and calculated the size and shape of the boundary in between domains, taking only material anisotropy and the exchange interaction into account. This work was further improved upon in 1935 by Landau and Lifshitz [9] by taking all the energy terms into account. Their insights not only advanced the understanding of domain walls but laid, in fact, the basis for all of the micromagnetism by deriving the (now famous) Landau–Lifshitz equation. This equation describes

the dynamics of magnetic moments while minimizing all of the energy terms. Following the work of Döring [10], the last step towards a complete framework of micromagnetism as it is still used today was performed by Gilbert [11]. He investigated a more physical description of damping in ferromagnetic materials and reformulated the Landau–Lifshitz equation as the Landau–Lifshitz–Gilbert equation (LLG).

This demonstrates that the theory of micromagnetism gradually grew during a time span of several decades. In the sixties, the elements for this complete framework were combined in a comprehensive overview [1] by Brown. Due to the complexity of the micromagnetic equations, only (relatively) simple problems can be solved analytically. The best-known example is still the domain wall calculation of Landau and Lifshitz [9]. Although it is possible to tackle complex systems by carefully analyzing and simplifying the micromagnetic equations (e.g. the 1D-model for domain wall motion by Schryer and Walker [12]), the field of micromagnetism did not advance very quickly. Only when increasingly faster computers became available did it become possible to numerically solve micromagnetic problems and compare their solutions to the corresponding analytical counterparts. Ever since, the field of micromagnetism has taken flight. Recently, the possibility to calculate on graphics cards [13, 14] has further increased the possibilities to perform faster, larger and more complex simulations.

1.2. Micromagnetic theory

In the micromagnetic formalism, the magnetization of a magnetic material is described by a continuous vector field \mathbf{M} . Usually, the norm of the magnetization vector at each point is assumed to be constant and equal to the saturation magnetization, M_s . Therefore, the reduced magnetization $\mathbf{m} = \frac{\mathbf{M}}{M_s}$, with $\|\mathbf{m}\| = 1$, is introduced to describe the direction of the magnetic moment at each point in space.

At the heart of micromagnetism lies the Landau–Lifshitz–Gilbert equation, which describes the spatial and temporal evolution of magnetization: a precession around and damping towards the local effective field, whose main contributions are described in section 1.2.1. In the absence of damping, the magnetization will indefinitely precess around the effective field,

$$\dot{\mathbf{M}} = -\gamma \mathbf{M} \times \mu_0 \mathbf{H}_{\text{eff}}, \quad (1)$$

with a precession frequency equal to

$$f = \frac{\gamma_0 \mathbf{H}_{\text{eff}}}{2\pi} \approx \mu_0 \mathbf{H}_{\text{eff}} 28 \text{ GHz T}^{-1} \quad (2)$$

where $\gamma_0 = 2.21 \times 10^5 \text{ m As}^{-1}$ is the product of the vacuum permeability μ_0 and the gyromagnetic ratio

$$\gamma = \frac{ge}{2m_e} \quad (3)$$

where e and m_e are the charge and mass of the electron, respectively, and $g \approx 2$ is the Landé factor.

In reality, however, energy is dissipated by, e.g. eddy currents and phonon excitations via the spin-lattice coupling.

Landau and Lifshitz [9] took this damping into account by adding a phenomenological torque to equation (1) which slowly directs the magnetization towards the effective field. The Landau–Lifshitz equation thus reads

$$\dot{\mathbf{m}} = -\gamma_0 \mathbf{m} \times \mathbf{H}_{\text{eff}} - \lambda \mathbf{m} \times (\mathbf{m} \times \mathbf{H}_{\text{eff}}). \quad (4)$$

In 1955, Gilbert [11] introduced a different approach to describe the damping. Also phenomenologically, but physically more intuitive, he assumed that the damping is proportional to the time derivative of the magnetization $\dot{\mathbf{m}}$, with α (the Gilbert damping parameter) as the proportionality constant. Typically, an α of 0.01 is measured in permalloy, but this value can be as high as 0.3 in materials with perpendicular magnetic anisotropy.

Using Gilbert's approach, the Landau–Lifshitz equation can be written in its Gilbert form (also called the Landau–Lifshitz–Gilbert equation)

$$\dot{\mathbf{m}} = -\gamma_0 \mathbf{m} \times \mathbf{H}_{\text{eff}} + \alpha \mathbf{m} \times \dot{\mathbf{m}}. \quad (5)$$

Although equations (4) and (5) look different, they can easily be transformed into one another by substituting λ and γ_0 in the Landau–Lifshitz equation by $\frac{\gamma_0 \alpha}{1+\alpha^2}$ and $\frac{\gamma_0}{1+\alpha^2}$, respectively.

1.2.1. Effective field contributions. The effective field can be written as the derivative of the magnetic energy densities to the magnetization

$$\mathbf{H}_{\text{eff}} = -\frac{1}{\mu_0} \frac{d\mathcal{E}}{d\mathbf{M}}, \quad (6)$$

where the different energies are calculated as a volume integral of the local energy densities \mathcal{E} over the total considered volume V

$$\mathcal{E} = \frac{dE}{dV}. \quad (7)$$

When one is interested only in statics (as opposed to dynamics which concerns itself with the time evolution of the magnetization), the equilibrium magnetization state can be found by minimizing the total energy E_{total} of the system.

A list of the most commonly considered energy terms contributing to the effective field is given below.

1.2.2. Zeeman energy. The Zeeman energy is the energy due to an externally applied magnetic field \mathbf{H}_{ext} , and is minimal when the magnetization is aligned with this field. The energy density is given by

$$\mathcal{E}_{\text{Zeeman}} = -\mu_0 \mathbf{M} \cdot \mathbf{H}_{\text{ext}}. \quad (8)$$

1.2.3. Exchange energy. The exchange interaction tries to align neighboring spins. It has a quantum-mechanical origin [4] as it results from the interplay between the Coulomb repulsion between different electrons and Pauli's exclusion principle. It can be derived from the Heisenberg exchange Hamiltonian

$$\hat{\mathcal{H}}_{\text{exch}} = -2\mathcal{J} \hat{\sigma}_i \cdot \hat{\sigma}_j. \quad (9)$$

In this equation, $\hat{\sigma}_i$ and $\hat{\sigma}_j$ are two neighboring electron spins, and \mathcal{J} is the strength of the exchange interaction. A positive

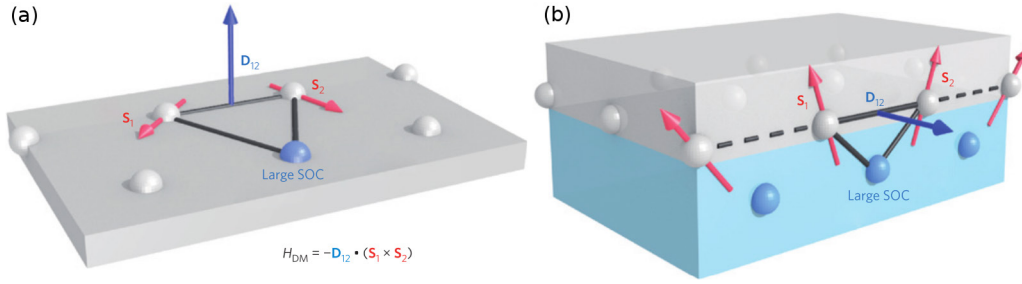


Figure 1. (a) Sketch of the DMI induced in the bulk of crystal with a non-centrosymmetric lattice. (b) Sketch of the DMI induced at an interface with a heavy metal layer and large spin-orbit coupling. Reprinted by permission from Macmillan Publishers Ltd: Nature Nanotechnology [16], Copyright 2013.

\mathcal{J} results in a ferromagnetically ordered material and when \mathcal{J} is negative it is possible to find a ferrimagnetic or antiferromagnetic ordering.

In the continuum limit of micromagnetism, equation (9) leads to an exchange energy density of

$$\mathcal{E}_{\text{exch}} = A_{\text{ex}} (\nabla \mathbf{m})^2 \quad (10)$$

where A_{ex} denotes the exchange stiffness constant and $(\nabla \mathbf{m})^2$ is shorthand for

$$(\nabla \mathbf{m})^2 = (\nabla m_x)^2 + (\nabla m_y)^2 + (\nabla m_z)^2. \quad (11)$$

Equation (10) physically means that there is an energy penalty whenever the magnetization is not uniform. Its competition with magnetostatic energy also sets a lower limit to the length scale of the variations in the magnetization, called the exchange length

$$l_{\text{ex}} = \sqrt{\frac{2A_{\text{ex}}}{\mu_0 M_s^2}}, \quad (12)$$

with $\mu_0 = 4\pi \times 10^{-7} \text{ Tm A}^{-1}$ the vacuum permeability. A typical exchange length in e.g. permalloy is 5.2nm. To vary the magnetization on a smaller length scale requires magnetic fields larger than M_s , which can only be obtained in magnetic materials when other effective field terms are playing. For example, magnetocrystalline anisotropy, discussed below, has a characteristic length scale given by

$$\kappa = \sqrt{A_{\text{ex}}/K}, \quad (13)$$

with K being the anisotropy constant.

Finally, the contribution to the effective field due to $\mathcal{E}_{\text{exch}}$ is given by

$$\mathbf{B}_{\text{exch}} = 2 \frac{A_{\text{ex}}}{M_s} \Delta \mathbf{m}. \quad (14)$$

1.2.4. Dzyaloshinskii–Moriya interaction. The Dzyaloshinskii–Moriya interaction [15] (DMI), induced by the spin-orbit coupling in ferromagnetic films with a lack or breaking of inversion symmetry, has a chiral character. This asymmetric interaction favors the canting of two neighboring magnetic moments in one direction over the other. This asymmetry is clearly reflected in the Heisenberg Hamiltonian which models the DMI interaction between atomic spin $\hat{\sigma}_i$ and $\hat{\sigma}_j$:

$$\hat{\mathcal{H}}_{\text{DMI}} = \mathcal{D}_{ij} \cdot (\hat{\sigma}_i \times \hat{\sigma}_j). \quad (15)$$

The lack of inversion symmetry can be found in ferromagnetic films with a non-centrosymmetric lattice or in layered heterostructures with ultra-thin ($< 2 \text{ nm}$) ferromagnetic layers and heavy metal layers with a strong spin-orbit coupling. In the latter case, one often uses the term *interfacially-induced DMI*. The orientation of the DMI vector \mathcal{D}_{ij} is determined by the type of DMI as shown in figure 1. This interaction stabilizes chiral spin structures such as domain walls, cycloids and spirals (contiguous domain walls), and skyrmions [17] (closed domain walls). In what follows, we limit ourselves to an overview of micromagnetic simulations of systems with an interfacially induced DMI. The continuization of the DMI Hamiltonian yields, for its interfacially-induced type, the micromagnetic energy density

$$\mathcal{E}_{\text{DMI}} = D [m_z (\nabla \cdot \mathbf{m}) - (\mathbf{m} \cdot \nabla) m_z] \quad (16)$$

with DMI strength $D \propto |\mathcal{D}|$. Note that the energy depends only on the gradient of the magnetization along the directions parallel to the interface.

This energy density

$$\mathcal{E}_{\text{DMI}} = -\frac{1}{2} \mathbf{M} \cdot \mathbf{B}_{\text{DMI}} \quad (17)$$

can be calculated easily starting from the corresponding effective field term

$$\mathbf{B}_{\text{DMI}} = \frac{2D}{M_s} \left(\frac{\partial m_z}{\partial x}, \frac{\partial m_z}{\partial y}, -\frac{\partial m_x}{\partial x} - \frac{\partial m_y}{\partial y} \right). \quad (18)$$

1.2.5. Magnetostatic energy. The magnetostatic energy is the energy of magnetic moments in the magnetic field resulting from all considered moments (including itself). This energy is minimized when all the flux loops are closed and there are no stray fields outside of the magnet.

$$\mathcal{E}_{\text{magnetostatic}} = -\frac{1}{2} \mathbf{M} \cdot \mathbf{B}_{\text{demag}}. \quad (19)$$

In equation (19), $\mathbf{B}_{\text{demag}}$ is the demagnetizing field

$$\mathbf{B}_{\text{demag}} = \frac{\mu_0}{4\pi} \int_V M_s \left[3 \frac{(\mathbf{m} \cdot \mathbf{r}) \mathbf{r}}{\|\mathbf{r}\|^5} - \frac{\mathbf{m}}{\|\mathbf{r}\|^3} \right] \mathbf{dr}. \quad (20)$$

This expression can be derived from Maxwell's equations [18] and shows that the demagnetizing field is the integral of all fields produced by all dipoles. The demagnetizing

field $\mathbf{B}_{\text{demag}}$ within a uniformly magnetized ellipsoid is uniform [18] and can be written as

$$\mathbf{B}_{\text{demag}} = -\mu_0 \mathcal{N} \mathbf{M}, \quad (21)$$

where \mathcal{N} denotes the so-called demagnetizing tensor.

The individual interaction between two dipoles is relatively weak, and is always smaller than the exchange interaction on short distances. However, unlike the exchange interaction which only acts between nearest neighbors, the magnetostatic interaction is a long-range interaction and is responsible for the formation of domains in magnetic materials. Another consequence of this long-range interaction is that micromagnetic calculations are computationally very challenging, which is discussed in further detail below.

1.2.6. Magnetocrystalline anisotropy energy. The structure of the crystal lattice can impose preferred directions on the magnetization via the spin-orbit coupling. The simplest example is called uniaxial anisotropy and gives rise to one preferred direction. The energy density for uniaxial anisotropy can be obtained starting from its effective field contribution,

$$\mathbf{B}_{\text{anis}} = \frac{2K_{u1}}{M_s} (\mathbf{u} \cdot \mathbf{m}) \mathbf{u} + \frac{4K_{u2}}{M_s} (\mathbf{u} \cdot \mathbf{m})^3 \mathbf{u} \quad (22)$$

and is thus given by

$$\mathcal{E}_{\text{anis}} = -\frac{1}{2} \mathbf{B}_{\text{anis}}(K_{u1}) \cdot \mathbf{M} - \frac{1}{4} \mathbf{B}_{\text{anis}}(K_{u2}) \cdot \mathbf{M} \quad (23)$$

$$= -K_{u1} (\mathbf{u} \cdot \mathbf{m})^2 - K_{u2} (\mathbf{u} \cdot \mathbf{m})^4. \quad (24)$$

$\mathbf{B}_{\text{anis}}(K_{ui})$ denotes the effective field term where only K_{ui} is taken into account.

The anisotropy constants (expressed in J m^{-3}) can be either positive or negative. When they are positive, the energy is minimized when the magnetization is aligned with the anisotropy direction \mathbf{u} , which is then called an easy-axis. When they are negative, the magnetization tries to align with the plane perpendicular to the anisotropy axis to minimize the energy, which is then called a hard-axis.

Next to the uniaxial one, a second frequently used magnetocrystalline anisotropy is cubic anisotropy, whose effective field term is given by

$$\begin{aligned} \mathbf{B}_{\text{anis}} &= -2K_{c1}/M_s (((\mathbf{c}_2 \cdot \mathbf{m})^2 + (\mathbf{c}_3 \cdot \mathbf{m})^2) ((\mathbf{c}_1 \cdot \mathbf{m}) \mathbf{c}_1) \\ &\quad + ((\mathbf{c}_1 \cdot \mathbf{m})^2 + (\mathbf{c}_3 \cdot \mathbf{m})^2) ((\mathbf{c}_2 \cdot \mathbf{m}) \mathbf{c}_2) \\ &\quad + ((\mathbf{c}_1 \cdot \mathbf{m})^2 + (\mathbf{c}_2 \cdot \mathbf{m})^2) ((\mathbf{c}_3 \cdot \mathbf{m}) \mathbf{c}_3)) \\ &- 2K_{c2}/M_s (((\mathbf{c}_2 \cdot \mathbf{m})^2 (\mathbf{c}_3 \cdot \mathbf{m})^2) ((\mathbf{c}_1 \cdot \mathbf{m}) \mathbf{c}_1) \\ &\quad + ((\mathbf{c}_1 \cdot \mathbf{m})^2 (\mathbf{c}_3 \cdot \mathbf{m})^2) ((\mathbf{c}_2 \cdot \mathbf{m}) \mathbf{c}_2) \\ &\quad + ((\mathbf{c}_1 \cdot \mathbf{m})^2 (\mathbf{c}_2 \cdot \mathbf{m})^2) ((\mathbf{c}_3 \cdot \mathbf{m}) \mathbf{c}_3)) \\ &- 4K_{c3}/M_s (((\mathbf{c}_2 \cdot \mathbf{m})^4 + (\mathbf{c}_3 \cdot \mathbf{m})^4) ((\mathbf{c}_1 \cdot \mathbf{m})^3 \mathbf{c}_1) \\ &\quad + ((\mathbf{c}_1 \cdot \mathbf{m})^4 + (\mathbf{c}_3 \cdot \mathbf{m})^4) ((\mathbf{c}_2 \cdot \mathbf{m})^3 \mathbf{c}_2) \\ &\quad + ((\mathbf{c}_1 \cdot \mathbf{m})^4 + (\mathbf{c}_2 \cdot \mathbf{m})^4) ((\mathbf{c}_3 \cdot \mathbf{m})^3 \mathbf{c}_3)) \end{aligned} \quad (25)$$

which again is used to obtain the energy density

$$\begin{aligned} \mathcal{E}_{\text{anis}} &= K_{c1} ((\mathbf{c}_1 \cdot \mathbf{m})^2 (\mathbf{c}_2 \cdot \mathbf{m})^2 \\ &\quad + (\mathbf{c}_1 \cdot \mathbf{m})^2 (\mathbf{c}_3 \cdot \mathbf{m})^2 \\ &\quad + (\mathbf{c}_2 \cdot \mathbf{m})^2 (\mathbf{c}_3 \cdot \mathbf{m})^2) \\ &+ K_{c2} ((\mathbf{c}_1 \cdot \mathbf{m})^2 (\mathbf{c}_2 \cdot \mathbf{m})^2 (\mathbf{c}_3 \cdot \mathbf{m})^2) \\ &+ K_{c3} (((\mathbf{c}_1 \cdot \mathbf{m})^4 (\mathbf{c}_2 \cdot \mathbf{m})^4 \\ &\quad + (\mathbf{c}_1 \cdot \mathbf{m})^4 (\mathbf{c}_3 \cdot \mathbf{m})^4 \\ &\quad + (\mathbf{c}_2 \cdot \mathbf{m})^4 (\mathbf{c}_3 \cdot \mathbf{m})^4) \end{aligned} \quad (26)$$

using

$$\mathcal{E}_{\text{anis}} = -\frac{1}{4} \mathbf{B}_{\text{anis}}(K_{c1}) \cdot \mathbf{M} - \frac{1}{6} \mathbf{B}_{\text{anis}}(K_{c2}) \cdot \mathbf{M} - \frac{1}{8} \mathbf{B}_{\text{anis}}(K_{c3}) \cdot \mathbf{M}. \quad (27)$$

In these equations, $\mathbf{c}_1, \mathbf{c}_2$ and \mathbf{c}_3 denote three mutually perpendicular anisotropy directions and K_{cn} is the n th-order cubic anisotropy constant.

1.2.7. Thermal fluctuations. The LLG equation (equation (5)) describes the magnetization dynamics at zero temperature. To investigate nonzero temperatures, the effects of thermal fluctuations should be taken into account.

To this end, Brown [19, 20] developed a theory when he investigated the thermal switching of single-domain particles using the fluctuation-dissipation theorem. In 1993 [21], it was realized that this theory was also applicable to micromagnetic simulations, by extending the effective field in the LLG equation with a stochastic thermal field, because each finite difference cell can be seen as a single-domain ‘particle’. The thermal field \mathbf{H}_{th} had the following properties:

$$\langle \mathbf{H}_{\text{th}} \rangle = 0 \quad (28)$$

$$\langle \mathbf{H}_{\text{th},i}(t) \mathbf{H}_{\text{th},j}(t') \rangle = q \delta_{\text{D}}(t - t') \delta_{\text{D},ij} \quad (29)$$

$$q = \frac{2k_{\text{B}} T \alpha}{M_s \gamma_0 \mu_0 V}. \quad (30)$$

The operator $\langle \cdot \rangle$ denotes an average over time, $\langle \cdot \cdot \rangle$ a correlation, δ_{D} the Dirac delta function and the indices i and j go over the x , y and z axes in a Cartesian system. k_{B} denotes the Boltzmann constant, T the temperature and V the volume in which the thermal fluctuations are considered. Physically, these equations tell us that the thermal field has zero average, is uncorrelated in time and space, and its size is determined by q .

These equations are determined in such a way that the effect of the thermal fluctuations is independent to the spatial discretization. For example, when splitting up a volume into two smaller volumes and comparing the thermal fluctuations with those on the whole volume, one will, on average, recover the same behavior. Similarly, as with larger volumes, when averaged out over a larger time, thermal fluctuations should become smaller. Again, this proportionality is determined so that the thermal fluctuations over long periods of time do not depend on the time discretization in the simulations.

The thermal fluctuations described above act on the same timescales as the other micromagnetic torques, i.e. picoseconds. However, when looking at, e.g. ensembles of nanoparticles, macroscopic measurements are unable to capture any of these dynamics as they are averaged out over many particles and longer timescales. The quantities of interest are not always the fast dynamics but the slower ones resulting from thermally driven jumps over energy barriers. Therefore, an alternative approach is to describe the effect of thermal fluctuations as a jump noise process [22–25], where, based on the energy landscape for each finite difference cell, the switching time and final magnetization direction are determined stochastically and only the resulting changes in the magnetization, instead of all random thermal fluctuations, are considered.

Finally, by construction, the Landau–Lifshitz or LLG equations conserve the norm of the magnetization. However, close to the Curie temperature, this is no longer physical. To account for these effects, a term perpendicular to the precession and damping terms can be added to the equations. This term describes the variations in the norm of the magnetization and allows the extension of micromagnetism to temperatures close to or even above the Curie temperature. The resulting equations, depending on the formalism used, are called the Landau–Lifshitz–Bloch [26] or Landau–Lifshitz–Baryakhtar equations [27].

These considerations are not only theoretically relevant, as recent technological advances such as heat-assisted magnetic recording [28] can only be simulated correctly with the inclusion of these terms. Although it is possible to investigate domain wall motion in these high-temperature regimes [29], mumax³ is restricted to temperatures well below the Curie temperature where the LLG equation is still valid.

1.2.8. Spin torques. Next to the energy terms contributing to the effective field, there exist several additional torque terms to take into account the interaction between the conduction electrons and the localized electrons responsible for the magnetization.

As predicted by Berger [30], a spin polarized current will exert a torque on the magnetization when the polarization is not aligned with the magnetization. Following Slonczewski and Berger [31–33], the torque resulting from current polarized in a layer with fixed magnetization can be expressed as

$$\begin{aligned} \tau_{\text{SL}} = & \beta \frac{\epsilon + \alpha\epsilon'}{1 + \alpha^2} (\mathbf{m} \times (\mathbf{m}_P \times \mathbf{m})) \\ & - \beta \frac{\epsilon' - \alpha\epsilon}{1 + \alpha^2} \mathbf{m} \times \mathbf{m}_P \end{aligned} \quad (31)$$

$$\beta = \frac{J_z \hbar}{M_s e d} \quad (32)$$

$$\epsilon = \frac{P(\mathbf{r}, t) \Lambda^2}{(\Lambda^2 + 1) + (\Lambda^2 - 1)(\mathbf{m} \cdot \mathbf{m}_P)}. \quad (33)$$

Here, J_z denotes the current density along the z axis, d is the free layer thickness, \mathbf{m}_P the electron polarization direction, P the spin polarization, the Slonczewski Λ parameter characterizes the spacer layer, and ϵ' is the secondary spin-torque

parameter. The Slonczewski torque is typically employed in spin torque oscillators to nucleate and sustain magnetization auto-oscillations.

When an unpolarized current enters a ferromagnet, it will quickly become polarized and will exert a torque when the local magnetization changes. Zhang and Li [34] proposed a theoretical framework applicable when such a spin-polarized current runs through a continuously varying magnetization profile. They added two spin-transfer torque terms to the LLG equation to arrive at

$$\begin{aligned} \dot{\mathbf{m}} = & \gamma_0 \mathbf{H}_{\text{eff}} \times \mathbf{m} + \alpha \mathbf{m} \times \dot{\mathbf{m}} - \mathbf{m} \times (\mathbf{m} \times [b\mathbf{J} \cdot \nabla] \mathbf{m}) \\ & - \beta \mathbf{m} \times [b\mathbf{J} \cdot \nabla] \mathbf{m}. \end{aligned} \quad (34)$$

In this equation, \mathbf{J} denotes the current density, β the degree of non-adiabaticity and

$$b = \frac{P\mu_B}{eM_s(1 + \beta^2)} \quad (35)$$

is a prefactor determined by M_s , P , the polarization of the spin-polarized current, e , the electron charge and μ_B , the Bohr magneton. The first spin-transfer torque term in equation (34) is called the adiabatic spin-transfer torque as it is assumed that the spin polarization adiabatically follows the magnetization, except for the small degree of non-adiabaticity taken into account separately in the second term. This is the non-adiabatic spin-transfer torque and is proportional to β . It is related to the spatial mistracking of moments between the conduction electrons and the local magnetization [34], and is also called the field-like torque [35] because its effect on the magnetization is similar to that of an externally applied field. The prominent consequence of the Zhang–Li torque is the current-driven domain wall motion.

Recently, alternative ways were also discovered to induce a spin-torque using currents. When a current passes through a metal layer with high spin–orbit coupling, the spin Hall effect can result in the injection of a spin current in the neighboring magnetic layer [36, 37]. Alternatively, an effective field can arise from the Rashba effect in layers with structural asymmetry [38]. Because these effects are the result of the spin–orbit interaction, they are called spin–orbit torques (SOT) and will add either a field or damping-like term to the LLG-equation (respectively, the first or second term in equation (5)).

1.2.9. Other energy and torque terms. Besides the terms listed above, other torques or energies might also contribute to the torque and energy equation. This can be the case when other order parameters are involved, e.g. ferroelectrics, or when there is an interaction with another material at an interface. When a ferromagnet is interfaced to an antiferromagnet, a local unidirectional effective field, called the exchange bias [39, 40] can occur. Later on, we will discuss how this can be included in a micromagnetic model.

2. Computational micromagnetics

As we mentioned above, the LLG equation (equation (5)) is a nonlinear integrodifferential equation that only permits

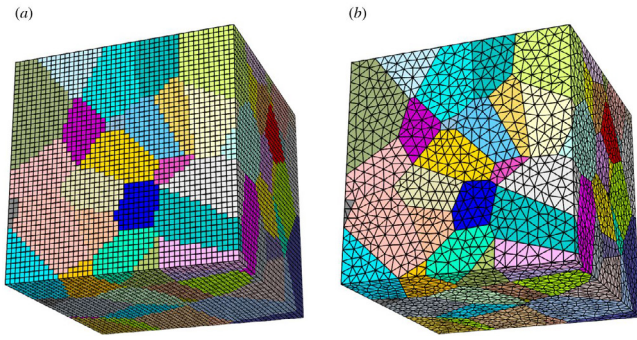


Figure 2. Comparison of the finite difference and finite elements discretization approaches. Reproduced from [41]. CC BY 4.0.

analytical solutions in a few corner cases. So, the majority of micromagnetic problems are solved numerically. The main challenge here is to calculate the right-hand side of the equation that contains effective magnetic field terms. This is typically achieved by discretizing the given problem in a certain way. Although local effective fields (those that only depend on the local value of the magnetic moment) are straightforward to calculate, the non-local ones, such as exchange and demagnetizing fields, require special numerical treatments.

2.1. Finite-difference versus finite-elements

In the finite difference method, one subdivides a given micromagnetic problem in a regular mesh of rectangular cuboids (see figure 2). Consequently, the spatial derivatives of the magnetization could be approximated using n -point stencils, which allows for the calculation of the exchange field [42] and Zhang-Li torques. Furthermore, as the magnetization is assumed to be uniform in every single cell of the simulation domain, its demagnetizing tensors could be relatively easily estimated using brute force dipolar summations, or the so-called Newell expressions [43]. The demagnetization field is then calculated using equation (21) and a convolution theorem that involves *six* fast Fourier transforms (FFTs) to bring the magnetization to the reciprocal space, perform local multiplication of the Fourier images of the demagnetizing tensors and magnetization, and transform the calculated field back to the forward space. An alternative approach based on the evaluation of the scalar potential was recently suggested [44, 45]. Although this scheme requires fewer FFT steps, it offers the same order of accuracy and performance as the tensor method explained above.

The finite-difference method is considered to be relatively fast, yet with low memory consumption, since only (a) the magnetization, (b) the right-hand side of the Landau–Lifshitz equation and (c) the Fourier image of the convolution kernel need to be stored. The main downsides of the finite difference method are (a) the inability to adequately approximate curved geometries (e.g. a sphere) and (b) reduced efficiency for sparse problems, as time-consuming calculations (e.g. FFT) have to be performed on empty cells.

These issues could be addressed with a finite-element method where the simulation domain is subdivided into so-called ‘elements’ as shown in figure 2 (typically triangles and tetrahedrons). Then, at the nodes of the obtained mesh, the solution of the given differential equation is approximated using an orthogonal basis (also known as interpolation functions), $\phi_i(\mathbf{r})$:

$$M^k(\mathbf{r}) = \sum u_i^k \phi_i(\mathbf{r}), \quad (36)$$

where i is the node number, k denotes a component of the magnetization and u_i^k are the values of the magnetization in the given basis. The local magnetic fields could be easily calculated in the given basis with $O(N)$ efficiency, while the exchange field could be calculated using the box method, i.e. as sparse matrix-vector products [46, 47]. As in the finite-difference method, the most computationally intensive part is the calculation of the magnetostatic field. Typically, it is estimated as the solution to the open boundary value problem

$$\Delta u = \frac{\nabla \mathbf{M}(\mathbf{r})}{\mu_0} \quad \mathbf{H}_d = -\nabla u, \quad (37)$$

that essentially reduces to the matrix-vector product

$$\mathbf{H}_d = \mathbf{Z}\mathbf{M}. \quad (38)$$

Since the kernel \mathbf{Z} is dense, the direct summation in equation (38) is computationally expensive. Instead, one can split the scalar potential into two parts: the one inside the magnet (which satisfies the Poisson equation) and the one outside the boundary of the magnetic region (which satisfies the Laplace equation) i.e. the so-called Fredkin and Koehler method [48]. The former is a solution of the sparse linear system, while the latter additionally requires an estimation of the dense matrix-vector product. This approach reduces the computational complexity of the magnetostatic field estimation, but its efficiency significantly drops, and its memory footprint increases if the problem is dominated by the boundary elements [47]. Although finite-elements methods are typically used to solve the LLG equation in the continuum approximation, a multiscale approach has been recently developed to obtain atomistic-scale resolution by coupling the Heisenberg lattice to the micromagnetic domain [49].

The time integration of the LLG can be performed using either implicit or explicit schemes. Traditionally, finite-difference micromagnetic solvers rely on the explicit Runge–Kutta methods, which provide satisfactory levels of precision and stability for the majority of dynamic micromagnetic problems. Also, they have relatively low computational complexity and memory consumption, since the solution is calculated as a linear combination of the subsequent magnetic torques. However, the finite-elements solvers typically rely on implicit methods. They offer outstanding stability and, compared to the same order explicit schemes, allow for large integration steps. At the same time, as implicit integration employs past values of the solution, sparse nonlinear systems have to be solved at every integration step. This comes at the cost of memory consumption and runtime, which might not be justified even by the larger integration steps.

It is worth mentioning that the integration of the stochastic LLG equation remains an open problem since some argue that only midpoint integration should be used to comply with the so-called Stratonovich calculus [50, 51], while Berkov [52] demonstrated that all the integration schemes are equivalent as long as the magnetization length is normalized after each integration step.

There is also a family of spectral methods that provide a solution to the Landau–Lifshitz equation in a reciprocal space and frequency domain. The best known are the dynamical matrix [53] and plane wave methods [54]. The idea is to assume a certain form of the solution to the LLG equation, e.g. by taking into account symmetry properties of the given problem. Upon the corresponding substitution, the LLG equation reduces to the eigenvalue problem, i.e. with no need for time integration. The main benefit of these methods is the direct access to the magnonic dispersion relation, spatial profiles of the eigenmodes and their relaxation rates [55], which typically require data analysis steps if time domain methods are used. Spectral methods are usually limited to the calculation of steady state linear magnetization dynamics, which, nevertheless, work well for the problems of magnonics.

2.2. GPU versus CPU

The emergence of general-purpose computing on graphical processing units (GPUs) enables faster and larger scale simulation in practically every research field. However, it is important to understand that doing calculations on GPUs is considerably more challenging than on central processing units (CPUs) for the following principal reasons:

- GPU performance excels in single precision calculus;
- GPUs have a limited amount of fast onboard memory;
- GPUs have significantly less sophisticated memory subsystems, e.g. cache amount per core, smaller register file, memory throughput per core, etc.

Although most of the CPU-based micromagnetic solvers rely heavily on double precision calculations, it becomes apparent that single precision is sufficient to solve even stiff standard micromagnetic problems [13, 56]. This could be attributed to the facts that (a) convolution kernels are typically calculated on the CPU side with extended precision, (b) GPUs make use of fused multiply-add instructions that effectively increase the accuracy of calculus and (c) special care is taken in the numerical algorithms to keep the quantities of the same order of magnitude. Nonetheless, if needed, one can either calculate some precision-sensitive components of the internal magnetic field (e.g. the exchange field) or even do the whole integration in double precision [45, 57, 58].

To overcome the limited amount of GPU onboard memory it is typically suggested to streamline the calculations, i.e. keep the data in the CPU memory and then transfer it to the GPU for processing and then back. As the connection between the CPU and GPU is rather slow and imposes high latencies, one needs to split the data into reasonable blocks and perform processing of the given block simultaneously with the

transfer of the others. This is a rather complex approach, so instead, the vast majority of the GPU-accelerated micromagnetic codes use an approach where all the data required for the integration of the LLG equation is stored entirely in the GPU memory. To allow for large-scale simulations, particular attention has to be given to keep the memory footprint of the simulations as low as possible.

By far, the most memory consuming part is the kernel required for the calculation of the demagnetizing field. In general, the convolution approach used in the finite difference method requires a 3×3 complex-valued tensor for every cell in the simulation domain. However, if symmetry properties of the demagnetization tensor are taken into account, its memory consumption could be reduced by a factor of 9 and 12 for 2D and 3D simulations, respectively [56]. In the finite-elements approach, the main idea is to keep all the kernels required for the calculations in sparse form. Nevertheless, even when the Fredkin and Koehler method is used, a dense matrix is needed for the calculation of the scalar potential in boundary elements. Instead, one might use non-uniform grid interpolation [46], hierarchical matrix-vector multiplication [57] or fast multipole [59] methods to effectively reduce this problem to the sparse matrix-vector product, which not only reduces memory requirements but also the computational complexity of the convolution to $O(N)$. Further optimizations could be made to decrease the amount of temporary data such as its on-the-fly recalculation (which might additionally offer performance benefits) or accumulation of the torque in a single data array unless the user requests its specific components. For example, a series of such optimizations allow mumax³ to simulate 3D structures with cells as large as 12×10^6 using less than 2 GB of GPU onboard memory. Similar scale problems could be accessed with finite-elements codes, although with significantly slower throughput.

Finally, although the raw computational power of both CPUs and GPUs substantially increases from one generation to another, the memory throughput available per each computational core shows much slower development. In fact, GPUs, having thousands of cores, are much more sensitive to this issue. This could be mitigated by either reducing the number of memory data transfers or by making sure enough calculations are done inbetween memory operations to hide their latency. However, micromagnetic codes typically perform matrix-vector products, stencils, FFTs, etc. that are intrinsically memory-intensive. In fact, figure 3 shows a virtually linear scaling of the mumax³ simulation performance with the GPU memory throughput, but not its raw computational power. Notably, the Nvidia GTX 580 GPU with raw computational throughput of 1.58 TFLOPS is only about $\times 3$ times slower than the 10 TFLOPS Nvidia Tesla P100, consistent with the corresponding difference in the GPU memory bandwidths. The situation becomes even more challenging given the complex memory hierarchy of modern GPUs and CPUs, e.g. caches of various levels, non-uniform memory access (NUMA), etc. So careful optimizations of the memory access patterns are ultimately required to achieve sufficient performance scaling of micromagnetic codes on both CPUs and GPUs [60–63].

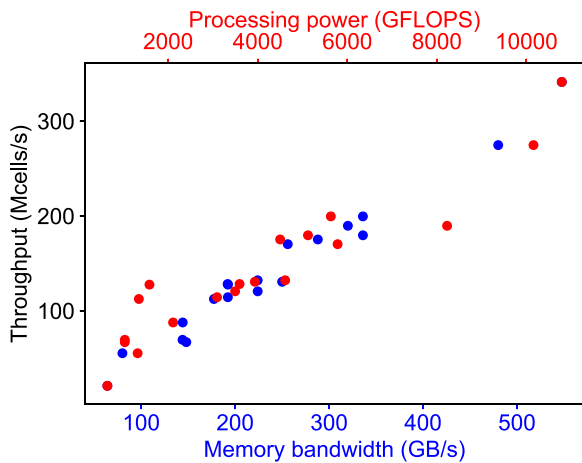


Figure 3. Scaling of `mumax3` throughput with GPUs raw single precision processing power and memory bandwidth measured by how many cells can have their torque evaluated per second (higher is better), for a simulation containing approximately 4 million cells.

2.3. Prominent GPU-accelerated micromagnetic solvers

Historically, the first finite-difference GPU-accelerated micromagnetic solver was developed by Lopez-Diaz *et al* in 2010, i.e. the so-called GPMagnet [13]. It is, however, still distributed in closed source form with a commercial license, which limits its adoption by the community. MicroMagnum [64] and Mumax [14] were the first public domain, free and open source solvers. All three are built using the Nvidia CUDA toolkit, which keeps them locked to the corresponding GPU vendor. This was addressed by Grace [58] and the code presented by Khan *et al* [65] that employs vendor-neutral C++ accelerated massive parallelism (C++ AMP) and open compute language (OpenCL) frameworks, respectively. GPU-accelerated versions of widespread CPU-based codes, LLG micromagnetics simulator and OOMMF, were also recently reported [45]. Finally, hotspin, a `mumax2` fork, remains the only GPU-accelerated solver that allows one to simulate longitudinal magnetization dynamics at finite temperatures [66].

The situation is dramatically different with finite-element solvers. While there are a few CPU-based codes actively used by the micromagnetic community, only two, not publicly available, GPU-accelerated solvers were reported so far: a GPU-enabled version of the TetraMag solver developed by Kakai *et al* [57] and FastMag reported by Li, Chang *et al* [46, 67]. Most likely, this could be attributed to the higher memory requirements and computational complexity of finite-element approaches as outlined above, so that only relatively small problems could be simulated on reasonable timescales. The situation will most likely change with the further development of the GPU distributed memory technology, which enables multiple GPUs to work efficiently on a single micromagnetic problem.

2.3.1. `mumax3`. The authors of this review contributed to the development of GPU-accelerated micromagnetic simulations by developing the software package `mumax3` [56]. It is based on the CUDA platform and optimized for performance and memory usage. It is capable of calculating systems of

over 16 million cells (on a GPU containing 6 GB memory). Special attention was dedicated to the flexibility of Mumax, which was achieved by the incorporation of powerful ways to define the system, supported by a website containing an API and examples. Novice Mumax users benefit from its intuitive and user-friendly graphical user interface, while those that are advanced have the freedom to define custom effective field terms and make use of the versatility of the Go programming language.

It was decided that Mumax will be distributed as freeware, which facilitated very high interest (in comparison with other similar programs) from the scientific community, resulting in more than 400 publications in which Mumax calculations are reported. Inspired by such a considerable interest, and in conjunction with the high number of research papers reporting results that have high relevance to further technological developments, the authors considered it timely and important to prepare a general review summarizing the use of Mumax and the contribution to magnetization studies achieved with this software.

We believe that performance is one of the key factors to the success of Mumax. Figure 4 demonstrates how its integration time of 10 ns long magnetization dynamics scales with the number of computational cells using 2D and 3D meshes. The benchmarks are done using the highest performance consumer-grade Nvidia GPU, i.e. Titan Xp. Practically, linear scaling is achieved in both cases, indicating an outstanding solver architecture which eliminates higher order (brute force) computational approaches. The scatter of the data is due to the size-dependent efficiency of the FFT and is common for both GPU and CPU implementations. As a rule of thumb, it is typically suggested to keep the mesh of $2^N \times 2^M \times 2^P$ size, where N, M, P are integers. Nevertheless, it can be seen that compared to 3D meshes, 2D meshes offer lower minimum integration times for the same total number of cells. This is due to the additional symmetries of the demagnetizing tensor being employed in the convolution as outlined above and 1/3 reduction in memory operation needed for the stencil calculations. The reduced memory pressure makes 2D simulations, on average, twice as fast compared to 3D when FFT-optimized meshes are used.

In contrast to CPU codes, Mumax does not need expensive hardware to demonstrate decent levels of performance. Figure 3 shows its computation throughput versus various kinds of consumer- and high-performance-computing- grade GPUs (measured by the number of cells evaluated per second for the 3D mesh containing 4M cells). The data demonstrates that the lowest performance mobile GPU we tested (i.e. Nvidia GTX650M, released in 2012) is about 17 times slower than the current highest performance GPU (i.e. Nvidia TESLA P100, released in 2016), while the present mass market device (i.e. Nvidia GTX 1070, released in 2016) is about two times slower.

To emphasize the benefits of the GPU-accelerated finite difference time domain micromagnetic simulations, we compare the performance of `mumax3` against the industry-standard, CPU-only OOMMF micromagnetic solver, which was extensively hand-tuned to scale almost linearly with the number

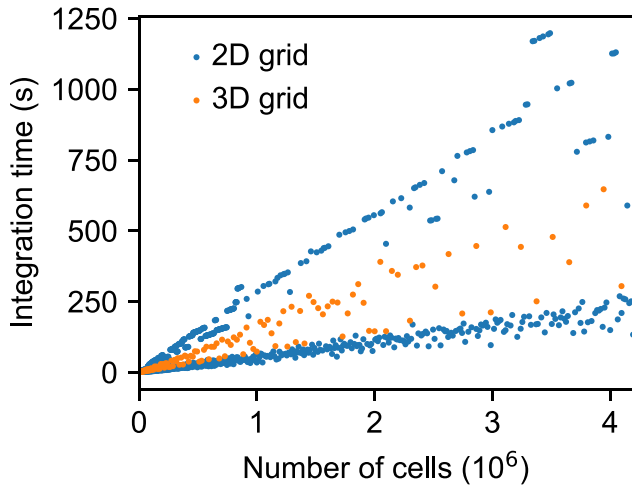


Figure 4. mumax^3 integration time versus number of simulated cells obtained for 2D and 3D grids, respectively.

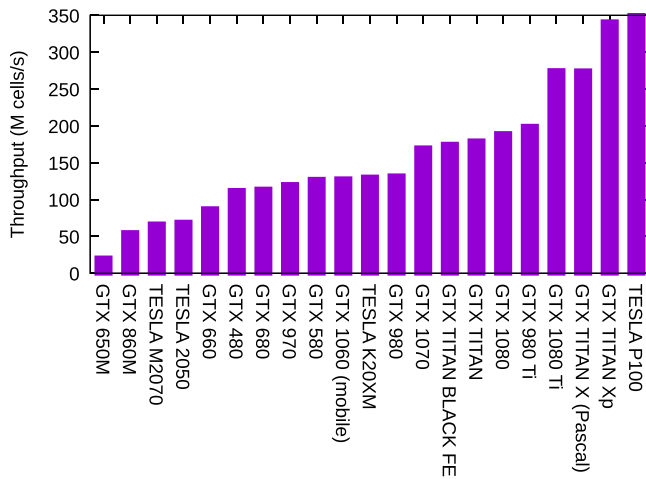


Figure 5. mumax^3 throughput for different consumer- and HPC-grade GPUs measured by how many cells can have their torque evaluated per second (higher is better), for a ≈ 4 million cell simulation.

of CPU cores [60]. Furthermore, we built OOMMF binaries with heavy compiler’s optimization, NUMA-awareness and with multi-threading enabled. We then consider two common computer configurations: (a) desktop-class, consisting of a Nvidia GTX 1070 GPU and Intel Core i5-2550K CPU (4 physical cores), and (b) workstation-class, consisting of a Nvidia Titan Xp GPU and 2x Xeon E5-2620 CPUs (16 physical cores in total). On the software side, we rely on the Fedora 27, Linux-based OS, GNU Compiler Collection 7.2.1 and Nvidia CUDA 9 toolkit. Then we integrate the very same 2D and 3D micromagnetic problem with both mumax^3 and OOMMF using identical solver configurations and measure the corresponding total runtimes using the GNU TIME command. The measured computational speedup of mumax^3 over OOMMF is shown in figure 6. It is visible that GPU-accelerated simulations could be about 200 times faster than the state-of-the-art CPU simulations, especially on large scale problems where GPU performance is used to its full capacity. Comparable speedups are obtained for 2D and 3D meshes

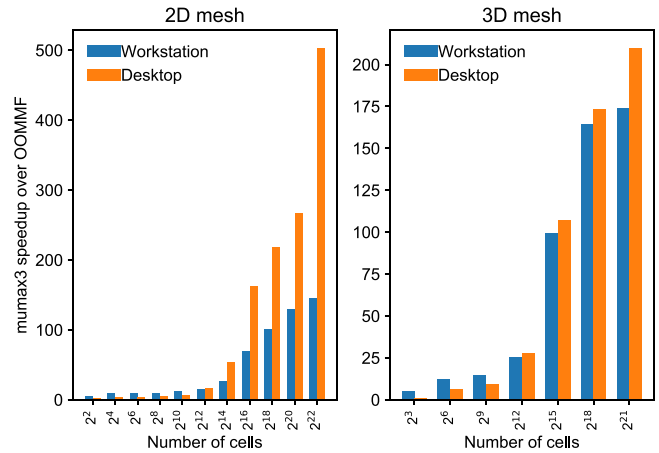


Figure 6. Runtime speedup of mumax^3 versus OOMMF2 for 2D and 3D meshes measured on desktop- and workstation-class computers.

indicating that the very same computational approaches and optimizations are employed in both packages. It should be noted that OOMMF performs calculations in double precision, which consumer-grade GPUs are rather slow at. This could be mitigated by using TESLA-class GPUs, but a factor of four reduction of GPU performance is expected as effectively a halved memory bandwidth, and half of the computational performance are available for the double precision calculations. Nevertheless, mumax^3 would still provide double-digit speedup over OOMMF. To conclude, it is evident that (a) GPU-accelerated computing is beneficial irrespective of the hardware type and (b) even the slowest performance mobile GPU (i.e, Nvidia GTX650M) provides a considerable speedup over CPU-only simulations using workstation-grade hardware.

3. Examples

This chapter gives a broad overview of how micromagnetic simulations, and more specifically the mumax^3 package [56], have been used in the last few years and we illustrate how this work has benefited from the performance increase of GPU acceleration.

3.1. Vortex core dynamics/switching

One of the simplest non-trivial configurations of soft magnetic thin film nanostructures is the vortex state with a whirling magnetization around an out-of-plane magnetized core. Since the discovery of the basic dynamic properties of vortices, i.e. the gyrotropic resonance [68, 69] and the vortex core switching dynamics [70, 71], these systems have been extensively studied. Most of the experimental studies relied on numerical micromagnetic modeling for the interpretation and validation of the results. However, the GPU accelerated codes allow for much more extended exploration within a wide parameter space, e.g. the parameter space for vortex core switching [72] or the modulation of the gyrotropic frequency through local geometric modulations [73, 74] and field modulations [75].

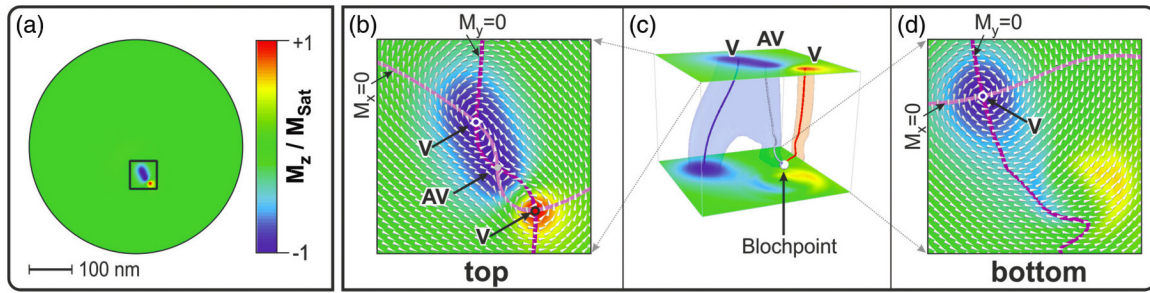


Figure 7. Illustration of the 3D nature of the vortex core switching process. (a) The simulated sample. (b) Top view of the top magnetization layer identifying the vortex-antivortex pair (blue) and the original vortex core (red). (c) Side view showing the Bloch point. (d) Top view of the bottom magnetization layer. Reproduced from [80]. CC BY 3.0.

A vortex state can also be created by the injection of a local spin polarized current in a thin magnetic film [76], and here GPU acceleration was also deployed to study an extensive phase space [77] and the influence of defects [78].

Most simulations on such thin film structures (with thickness typically below 50 nm) use a 2D discretization (only one cell in the out-of-plane direction). Although this approach captures most of the physics of these systems, care has to be taken as some processes have an intrinsic 3D character. When the gyrotropic mode of a vortex is excited, the vortex core polarity can be reversed by the dynamic creation of a vortex-antivortex pair and the consequent annihilation of a vortex [70], a process that involves a micromagnetic singularity (Bloch point). Particular care has to be taken when the dynamics of such a Bloch point need to be captured [79]. 3D discretization with small cell size, and consequently a large number of cells, will be required and GPU accelerated simulations are optimal. Noske *et al* [80] have investigated in detail the vortex reversal process for symmetric and asymmetric excitations. They showed that in all cases a Bloch point is involved and that in general, the magnetization is non-uniform in the out-of-plane direction (see figure 7).

3.2. Domain wall motion and creep

3.2.1. Introduction to domain wall motion. Domain walls and their dynamics are one of the main topics in micromagnetism [9]. Domain walls are regions where the magnetization rapidly changes direction, separating uniformly magnetized domains. These structures occur naturally in sufficiently large samples due to the interplay between the demagnetizing field and other effective-field terms.

Externally applied magnetic fields promote the growth of domains aligned parallel to the field at the cost of domains that point in the opposite direction. In particular, the motion of domain walls through thin nanostrips has received much interest because of its relative simplicity. This made it possible to study it analytically [10] in the early days of micromagnetism by reducing the Landau–Lifshitz equation to an equation describing the motion of domain walls. Similar to the Thiele equation, mainly used in vortex dynamics [68], this approach requires assumptions to be made on the domain wall shape and size, reducing it to a point object moving through a one-dimensional line. Hence, these models were called 1D

models. The first micromagnetic simulations aimed to validate and refine such a model [12]. As simulations increased in complexity over the years [81, 82], these 1D-models were also extended [83–85] and remain an important tool today to gain further insights into domain wall motion [86–88]. Magnetic field driven domain wall motion has the disadvantage that it requires relatively large magnetic fields, which are hard to apply only locally and thus it is difficult to use this mechanism in technological applications. Furthermore, because this driving mechanism does not directly act on the domain walls, but on the domains inbetween, it is possible for domain walls in the same nanostrip to move in opposite directions, collide, and annihilate, thus destroying the domain (wall) structure.

Besides magnetic fields, electric fields can also act as a driving force for domain walls [89–91] in suitable multiferroic heterostructures, such as a soft magnetic layer grown on a ferroelectric substrate consisting of several domains with alternating polarization. The magnetic domain walls are firmly pinned to the ferroelectric boundaries due to the strong anisotropy changes. When applying an electric field, the ferroelectric domain boundaries move, and the magnetic domain walls are pulled with them. As mumax³ is not a multiphysics package, it is not possible to include the substrate in the simulations. However, it can be accounted for by shifting the anisotropy properties within a simulation of the ferromagnet to observe how the domain wall moves along with this anisotropy boundary [90].

A second important domain wall driving mechanism is the spin-transfer torque exerted by a spin-polarized current running through a nanostrip [34, 92]. In contrast to the contributions to the effective field, the spin-transfer torque is not derived from an energy density but is included in the LLG equation directly as an additional torque term [35]. For these torques to be large enough to move the domain walls at an appreciable speed, typically large current densities are necessary ($>1 \text{ A } \mu\text{m}^{-2}$). Due to excessive Joule heating, such current densities can only be applied in very short pulses. Nevertheless, this driving mechanism has the advantage that it can drive all domain walls encountered in the nanostrip in the same direction, making this an excellent candidate for practical applications.

Finally, spin waves (described in detail in section 3.4) have been shown to act as a driving force for domain walls, either via direct excitation [93] or indirectly, via thermal gradients [94].

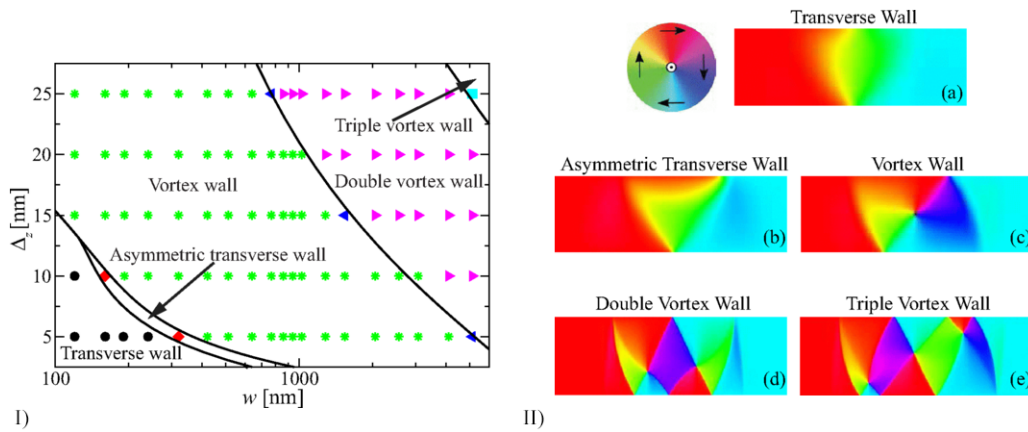


Figure 8. (I) Phase diagram of the equilibrium DW structure in permalloy strips of various thicknesses and widths. The symbols correspond to observations of the various equilibrium DW structures, with phase boundaries shown as solid lines. (II) Examples of the different equilibrium micromagnetic DW structures corresponding to the five different phases: (a) transverse domain wall, (b) asymmetric transverse domain wall, (c) vortex domain wall, (d) double vortex domain wall, and (e) triple vortex domain wall. The color wheel (top left) shows the mapping between the magnetization directions and colors. Reprinted figure with permission from [97], Copyright 2015 by the American Physical Society.

The remainder of this section will focus on the different domain walls found in materials with different material parameters and geometries and will be restricted to the main domain wall driving mechanisms: externally applied magnetic fields, spin-polarized currents or a combination of both [85, 95].

3.2.2. Domain wall types. The equilibrium configuration of a domain wall is determined by the detailed balance of the different magnetic interactions. Due to the 3D nature of magnetic systems, multiple types of domain walls exist and predicting which is the equilibrium configuration is not easy. One usually has to resort to micromagnetic simulations, and here fast GPU-accelerated simulators enable the exploration of extended phase spaces.

Thin films of materials with a weak or absent magneto-crystalline anisotropy will favor the magnetization to lie in the plane of the film. The most commonly used material is permalloy, an alloy consisting of roughly 80% nickel and 20% iron specifically designed to minimize magnetoelastic effects and which has no magneto-crystalline anisotropy. Figure 8 shows the phase diagram of the different domain wall types in nanostrips made out of this material. Depending on the width and thickness, the equilibrium domain wall is a transverse wall, a vortex domain wall [96], or in very wide nanostrips, even double or triple vortex domain walls [97–99]. Indeed, in wide strips, the shape anisotropy has less pronounced effects, favoring flux-closure states containing multiple vortices. Furthermore, a significant number of metastable domain wall structures can be found in these large strips [97, 100].

In nanostrips consisting of materials with large perpendicular magneto-crystalline anisotropy (PMA), either Bloch or Néel walls can be found (as shown in figure 9), with a preference for Bloch walls in thinner nanostrips. In the presence of an interfacially induced DMI (see section 3.3), the equilibrium structure becomes increasingly Néel-like [101, 102]. In contrast, the DMI induced in the bulk prefers domain walls with a Bloch character.

3.2.3. Field-driven domain wall motion. To understand the physical mechanism behind the motion of all these domain walls, simulations are an indispensable tool, because only very few direct dynamical experimental observations exist [103]. When looking at the domain wall velocity of a field-driven transverse wall [104] (see figure 10(a)), the following behavior is found. At low fields, the velocity increases almost linearly with the external field. For wider nanostrips, in which the equilibrium structure is a vortex domain wall, the vortex core is pushed out of the nanostrip, resulting in a transverse domain wall structure and an almost identical mobility curve.

At larger fields, a sudden drop in the domain wall velocity, called the Walker breakdown [12], is observed. This breakdown corresponds to the field at which it is no longer possible to reach a dynamical equilibrium, in which the out-of-plane torques are compensated by the demagnetizing field originating in the out-of-plane tilting of the domain wall. What happens physically in this dynamical regime depends on the equilibrium domain wall structure and thus the nanostrip size. In narrow nanostrips, an antivortex core is nucleated, which then traverses the nanostrip to annihilate at the other side. At this point, the domain wall again is a transverse configuration but with an oppositely pointing magnetization direction. Subsequently, a new antivortex core is nucleated, now with opposite polarity, which again traverses the nanostrip to annihilate at the other side. Above the Walker breakdown, the domain wall thus displays periodic transformations between an antivortex and a transverse domain wall configuration while it is driven forward.

In wider nanostrips, corresponding to the green dots in the phase diagram shown in figure 8, something similar is observed. However, the equilibrium domain wall is a vortex domain wall. Here, the vortex core is pushed out of the nanostrip, and the domain wall transforms into a transverse domain wall. Afterwards, a new vortex core (again with opposite polarity) nucleates and is pushed to the other side of the domain wall where it annihilates again. To summarize, the domain wall displays periodic transformations between a

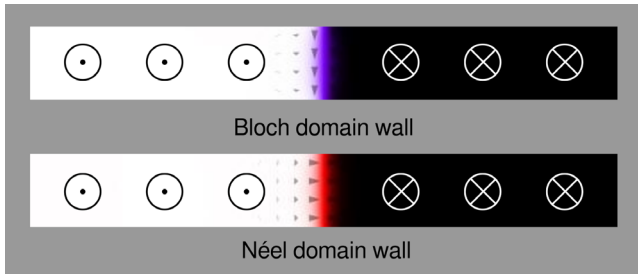


Figure 9. Examples of a Bloch and Néel type domain wall in a PMA nanostrip. The white/black color depicts the out-of-plane magnetization direction.

vortex domain wall and a transverse domain wall configuration during its forward motion [105, 106].

In nanostrips that are over $1\mu\text{m}$ wide, corresponding to the rightmost region of the phase diagram shown in figure 8, double or triple vortex domain walls are the equilibrium structure. There, the dynamics strongly depend on the system geometry, and in some cases, compact domain walls cannot be supported at all during the motion [98]. This is the case when different domain wall components acquire different propagation velocities, and the domain wall increases size indefinitely. In other cases, starting from a certain threshold field, the vortex core dynamically switches polarity close to the nanostrip edge via a double switching mechanism, leading to a high-velocity plateau at large external fields [99], contrasting the velocity drop typically observed above the Walker breakdown for narrower nanostrips. In these complex structures especially, the dynamics can no longer be reduced to simple models, and micromagnetic simulations are the only available tool to study the dynamics.

The field-driven motion of domain walls in materials with PMA is similar to the motion in in-plane materials. Below the Walker breakdown, the domain wall keeps its equilibrium Bloch structure, and its velocity depends linearly on the applied magnetic field. Above the Walker breakdown, the velocity drops suddenly as the domain wall structure periodically switches between a Bloch and Néel configuration, corresponding to a continuous rotation of the magnetization angle [87]. When the material also has a strong DMI, the mobility curves are qualitatively similar, i.e. a linear regime is found up to the Walker breakdown, but the DMI can further stabilize the domain wall and suppress the Walker breakdown up to higher applied fields and thus higher velocities [101]. The field driven motion of Dzyaloshinskii domain walls can be accurately described by a 1D-model, but an extra parameter is required to take the DMI-induced magnetization tilt into account [88].

3.2.4. Spin-transfer-torque (STT) driven domain wall motion. Spin-transfer-torque driven domain wall motion is similar to field-driven domain wall motion for transverse domain walls [92], see figure 10(b). The characteristics of the domain wall motion are largely determined by the degree of non-adiabaticity β . The adiabatic case ($\beta = 0$) shows an intrinsic depinning current threshold below which the domain wall is not moving. Similarly, as in the field-driven case,

below the depinning current threshold the vortex domain wall transforms into a transverse domain wall in which the effective field torques balance the adiabatic spin-transfer torques resulting in zero net torque, and consequently no movement. Above the depinning current, the adiabatic spin transfer torques are too large for the transverse domain wall to adapt its internal structure to balance the spin transfer torques. Consequently, the transverse domain wall becomes unstable, and a vortex core is nucleated and travels towards the opposite transverse direction, while moving along the strip as shown in figure 11(a), resulting in a periodic domain wall movement.

When a non-adiabatic contribution to the spin transfer torque is added with $\beta > \alpha$, two velocity regimes are separated by the Walker breakdown. However, as shown in figure 11(c), above the Walker breakdown the vortex core with a certain polarity moves in the opposite transverse direction, as compared to the $\beta = 0$ case.

When $\beta = \alpha$ (figure 11(b)), the adiabatic and non-adiabatic transverse torques balance each other, resulting only in a longitudinal vortex movement along the strip axis. In wider nanostrips, the mobility curves are similar, but in this case, the high-velocity regime physically originates in a double-vortex switching mechanism [99].

Similar to the field-driven case, current-driven domain wall dynamics in PMA materials closely follows the trends observed in in-plane materials: the domain wall velocity depends linearly on the current density (while remaining pinned in the case $\beta = 0$), up to an intrinsic depinning threshold or a Walker breakdown, depending on the degree of non-adiabaticity. For larger current densities, the domain wall structure again switches periodically between a Néel and Bloch like structure. In the presence of DMI, the domain wall motion becomes more complicated due to the appearance of a second steady-state motion with different properties, and the internal details of the domain wall determine which state will be reached [107]. Nevertheless, mainly at large current densities, there seems to be good agreement between the experimental results and micromagnetic simulations [108].

For wide PMA strips, the Walker breakdown corresponds to the nucleation of in plane-domains within the Bloch domain walls [109]. These ‘walls within walls’, in their turn, also display a rich mobility behavior, with a notable feature that these walls do not appear to show a Walker breakdown at high velocities, both for field and current driving mechanisms.

3.2.5. Spin-orbit-torque (SOT) driven domain wall motion. More recently, the possibility to drive domain walls with spin orbit torques (introduced in section 1.2.8) started to gain attention [110]. In contrast to the currents necessary for spin transfer torques, which always have to flow in the magnetic nanostrip itself in order to induce motion, spin orbit torques allow for much more degrees of freedom in the geometry and current direction. A detailed overview is given in [111]. The authors investigated two types of spin orbit torques: one due to the spin Hall effect, and one due to the Rashba effect. The former can be described by a Slonczewski torque (the first term in equation (31)), while the latter gives rise to a field-like torque (the second term in equation (31)).

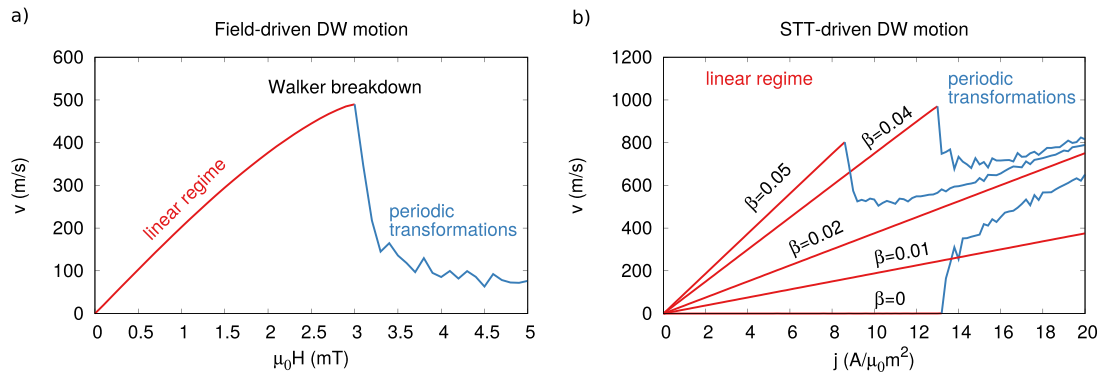


Figure 10. The velocity as a function of the driving force for a domain wall driven by (a) an externally applied magnetic field, (b) spin transfer torque with various degrees of nonadiabaticity, β . All simulations were performed on a transverse domain wall with a cross-sectional diameter of 10 nm by 100 nm, with $M_s = 860 \text{ kA m}^{-1}$, $A_{\text{ex}} = 13 \text{ pJ m}^{-1}$ and $\alpha = 0.02$.



Figure 11. The path of a vortex core in a permalloy nanostrip where the vortex domain wall is driven above the Walker breakdown/depinning current threshold by a spin-polarized current with (a) $\beta = 0$, (b) $\beta = \alpha$ and (c) $\beta = 2\alpha$.

The effect of these torques on three types of domain walls were investigated: Bloch and Néel walls in a PMA material and head-to-head domain walls in an in-plane magnetized material. Furthermore, this study was repeated for a parallel and a perpendicular geometry. The domain wall types and geometries are shown in figure 12.

This numerical study confirmed the simple explanation from geometric arguments that in the perpendicular geometry, either the spin Hall effect working on a Bloch wall, or the Rashba effect working on a head-to-head domain wall, resulted in a sustained motion, while in the parallel geometry only the spin Hall effect working on a Néel wall gives rise to a steady motion. For several reasons the latter case is very promising. Firstly, the DMI has a tendency to stabilize Néel domain walls, so that this type of driving mechanism is particularly suited for the high DMI materials currently studied, and second, much smaller current densities are required to obtain high domain wall velocities. Interestingly, depending on the material parameters, the motion of the domain wall can be either with or against the direction of the current flow [112]. These observations are confirmed by a study based on a 1D model taking SOTs into account [113].

3.2.6. Material disorder. Up to now, only nanostrips in the absence of structural disorder or thermal fluctuations were described. To correctly interpret experimental observations by comparing them to micromagnetic simulations, it is apt to try to take these effects into account as well.

The first studies taking disorder into account focused on edge roughness [82, 114, 115]. Such a disorder was shown to positively influence the domain wall motion by suppressing the

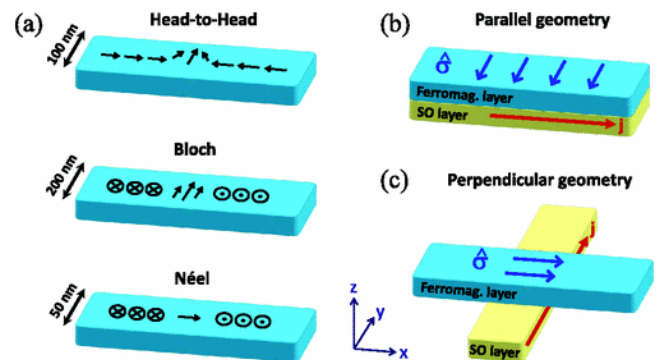


Figure 12. (a) The three types of domain walls under consideration in the numerical study. (b), (c) The two geometries under study, in which the ferromagnetic layer (F) lies parallel or perpendicular, respectively, to the SO layer through which the current flows. Reprinted figure with permission from [111], Copyright 2013 by the American Physical Society.

Walker breakdown in favor of a high-velocity plateau [82] not found in non-disordered nanostrips. Next to edge roughness, disorder distributed within the strip is also found in real wires due to defects in their microstructure like material grains. Such a disorder was first implemented into micromagnetic simulations by including empty finite-difference cells in the bulk of the material, leading to similar conclusions about the domain wall velocity [116] as the ones found in the presence of edge roughness. To improve upon the method to include material defects in the simulations, it was investigated how experimental characterizations of material defects [117–119] could be reproduced in simulations. Typically, defects give rise to a potential well, characterized in terms of a depth between

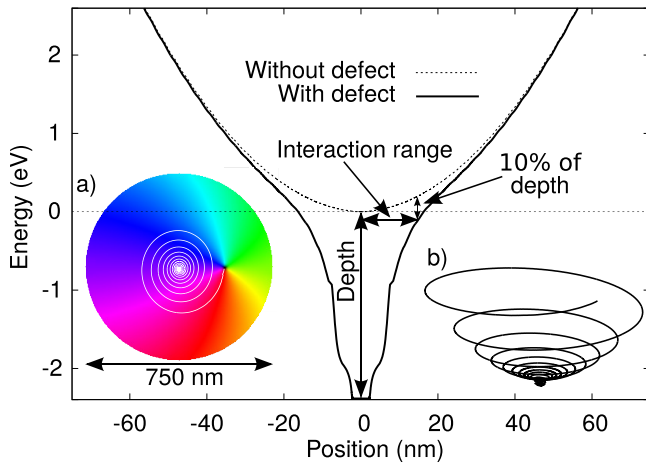


Figure 13. The magnetic energy of a vortex in a disk with (full line) and without (dotted line) a defect, implemented as a region in the center with a reduced exchange stiffness constant at the boundaries. Without the defect, the energy profile has a parabolic shape. The defect causes an additional potential well, for which the depth and interaction range are shown. Inset (a) depicts the initial magnetization in the disk and the trajectory the vortex core follows while it relaxes into the defect. Inset (b) depicts the energy of the system. Reprinted with permission from [121]. Copyright 2014, AIP Publishing LLC.

1–5 eV [117–119], and an interaction range of approximately 20 nm [117, 119, 120], corresponding to the size of the vortex core used to determine this range. In [121], a defect was introduced in the central region of a permalloy disk, as shown in figure 13(a). A magnetic vortex core was then inserted away from the center, and its trajectory was followed during its spiraling relaxation motion, during which the energy of the system is recorded. This energy is then used to determine the potential well properties. The resulting characterization was then utilized in a parameter study to identify the most realistic way to include defects.

In contrast to these isolated defects, the disorder can also exist on the level of material grains in polycrystalline materials. These are crystalline materials without long-range lattice order, originating in the way most thin films are grown: material grains grow outward from a few initial seeds until they encounter neighboring grains. [122, 123] present methods to simulate the complete grain structure of polycrystalline materials in a computationally efficient way using a Voronoi tessellation, in which each Voronoi cell represents a grain. An example of the resulting grain structure is depicted in figure 14. The implementation in mumax³ is described in detail in [123] and allows grains that previously left the simulation window to re-enter.

Having subdivided the geometry, one can vary the local material parameters in and between the grains. This way, grain-dependent anisotropy directions can represent the different lattice orientations in grains. The other possibilities are a grain-dependent saturation magnetization representing thickness variations between grains [124], and a reduced exchange stiffness constant at the grain boundaries representing a reduced magnetic coupling between neighboring grains [122]. In PMA materials, the angle and strength of the magnetocrystalline anisotropy may also be varied [122, 125].

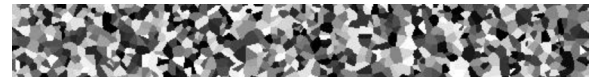


Figure 14. An example of a nanostrip with a surface of 1600 × 200 nm² subdivided into Voronoi cells (gray scale) with an average diameter of 20 nm. Reprinted with permission from [123]. Copyright 2014, AIP Publishing LLC.

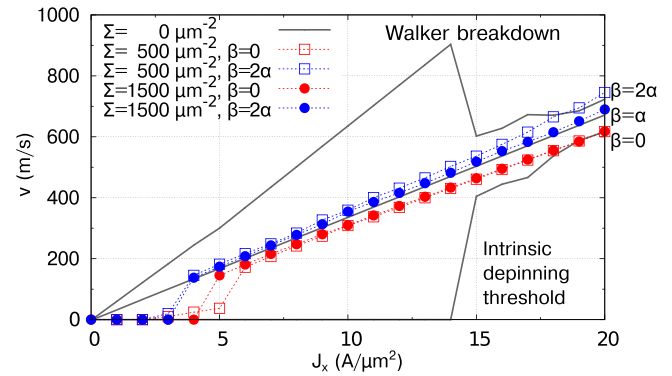


Figure 15. Velocity versus applied current density for a vortex domain wall. Solid lines: velocity versus applied current density in a nanostrip without disorder ($\beta = 0$, α and 2α). Colored symbols: velocity versus applied current density in nanostrips with disorder for $\beta = 0$ (red) and $\beta = 2\alpha$ (blue). Irrespective of the value of β used, the velocity curves tend to converge to a case corresponding to $\beta = \alpha$ in perfect strips. For small applied current densities, extrinsic pinning of the vortex core on a defect takes place. Reprinted figure with permission from [106], Copyright 2014 by the American Physical Society.

The influence of disorder on current-driven domain wall motion has been investigated in detail because this motion heavily depends on the size of the degree of non-adiabaticity β . There was a lot of debate on the magnitude of β in equation (34), with theoretically predicted values ranging from $\beta \approx \alpha$ to $\beta = 4\alpha$ [34, 84, 126–128]. Electrical and magnetic imaging techniques show domain wall transformations when a spin polarized current is applied, indicating β must be different from α [92, 129, 130]. However, experiments did not converge to one value, and found values of β/α ranging between 1 and 10 [131–141]. In [106], these discrepancies are explained by the influence of disorder. Commonly used experimental techniques to quantify β/α are based on distance measurements of a domain wall moved by a current pulse of known amplitude and duration. The resulting velocity is then compared to the theoretical and/or simulated values for different β s to determine β [138–141].

Comparing the domain wall velocity in the disordered nanostrips (colored lines in figure 15) to the non-disordered nanostrip case (black lines) it was observed that the intrinsic depinning current threshold (adiabatic case), as well as the Walker breakdown (non-adiabatic case), are suppressed, and the domain wall velocity is similar to the one for $\beta = \alpha$ in the case of non-disordered nanostrips. The origin of this different behavior was attributed to the interplay between the defects and the vortex domain wall. In a disordered nanostrip, the vortex core can switch polarity at a defect, implying a change in the lateral propagation direction and thus hindering the formation of the transverse domain wall. Such polarity switches

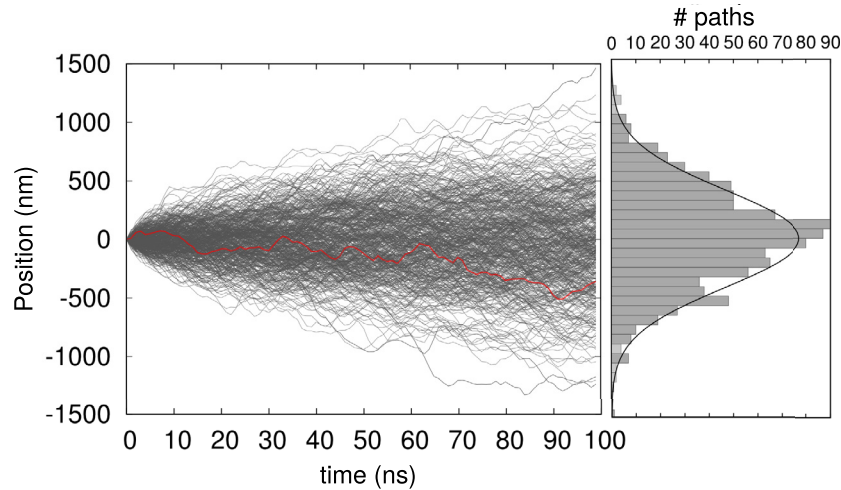


Figure 16. The left side of the figure shows the positions as a function of time for 1000 domain walls in a magnetic nanostrip at 300 K. One randomly chosen path is highlighted in red. The right side shows the distribution of their final positions, with a fitted Gaussian curve centered at 0, proving that the diffusive motion has no average displacement. Reprinted with permission from [143]. Copyright 2015, AIP Publishing LLC.

happen via a Bloch point, a detailed discussion of which can be found in section 3.1. In the experimentally accessible current range, the vortex core thus moves in the central region of the strip without the formation of transverse domain walls. This motion is similar to the motion of a vortex domain wall in a perfect strip for the case $\beta = \alpha$, which explains the deviating value of β/α derived from the domain wall motion. This was also corroborated by simulation studies of domain wall motion in polycrystalline permalloy [123]. A second conclusion that can be made from the data presented in figure 15 is that below an extrinsic depinning current threshold, the domain wall velocity becomes zero in disordered nanostrips. This is explained by the fact that the driving force is not sufficiently large to overcome the energy barriers due to the disorder, and the domain walls get pinned to the disorder.

Voto *et al* [125] presents the results of domain wall motion through a polycrystalline PMA strip, and finds that the disorder gives rise to higher velocities in the high-field regime, which could be attributed mainly to the local variations in the anisotropy axes orientation. These findings stress the fact that different methods to include disorder in the simulations can give rise to various effects on the mobility [121, 125] and one should be careful in choosing the correct method to reproduce or interpret experimental results.

3.2.7. Nonzero temperature. The influence of temperature on transverse domain wall dynamics in magnetic nanostripes is also a topic of interest [142, 143]. Temperature is included in the micromagnetic simulations and the 1D-model as a randomly fluctuating field acting on the finite difference cells and domain wall volume, respectively. As shown in figure 16, the combined action of thermal fluctuations and current do not give rise to an average domain wall motion. Instead, the data is described by a Gaussian curve with zero average. Consequently, the motion can be interpreted as a random walk resulting in diffusion and characterized by a mean square displacement. In general, the domain wall motion contains a drift and a diffusion component which can be quantitatively predicted by the 1D-model extended with a thermal field.

Finally, the most realistic simulations investigate the interplay between disorder and thermal fluctuations on domain wall motion. There is an inherent stochasticity [114, 144] in this motion, which makes it impossible to accurately predict when and for how long a domain wall will get pinned in a nanostrip, even with perfect knowledge about the magnetization history. However, when looking at the average motion of domain walls in this regime, it is possible to make quantitative predictions [145]. Typically, elastic systems in disordered media, such as domain walls in ferromagnets [146, 147], are pinned at zero temperature. At temperatures smaller than the depinning temperature and forces smaller than the depinning force, they exhibit a creep [148] regime originating in the slow thermally activated motion over large energy barriers, leading to a highly non-linear creep scaling law. In particular, for 1D elastic lines such as domain walls in ferromagnetic thin (PMA) films, compelling evidence for the validity of this scaling law exists [146, 147]. Kim *et al* [149] experimentally showed that in PMA materials the creep scaling law breaks down when the nanostrip dimensions are reduced. In [150], this behavior was further investigated for narrow polycrystalline nanostrips with the help of micromagnetic simulations.

The results of this study are shown in figure 17, where each data point shows the average domain wall velocity over five simulations with different temperature realizations. The panels on the right show the domain wall paths for some representative current densities. In the flow regime (e.g. $J_x = 4 \text{ A } \mu\text{m}^{-2}$), neither the disorder nor the thermal fluctuations have a noticeable effect on the domain wall motion. At intermediate current densities, in the depinning regime (e.g. $J_x = 1 \text{ A } \mu\text{m}^{-2}$), only a small number of pinning potential wells are strong enough to temporarily pin the domain wall. This introduces some variance in the domain wall velocities. In the creep regime (e.g. $J_x = 0.1 \text{ A } \mu\text{m}^{-2}$), the domain walls repetitively pin for several microseconds, resulting in average domain wall velocities down to 1 m s^{-1} .

To further address this low current density regime, the 1D model was extended with thermal fluctuations and a term taking into account the energy landscape due to the

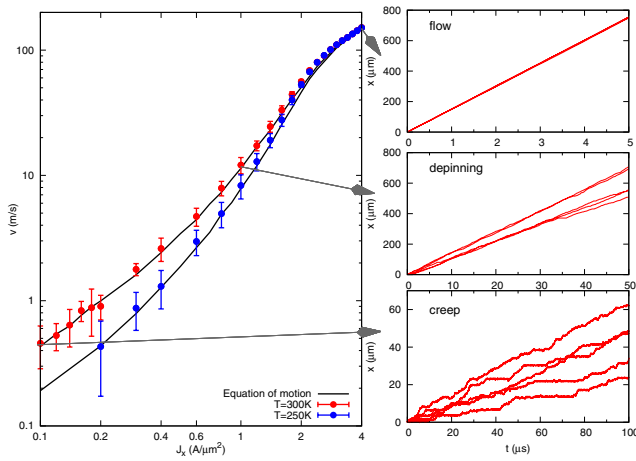


Figure 17. Micromagnetic simulations of current-driven transverse domain wall motion reveal a low-current density creep regime, and allow one to validate the equation of motion of the domain wall. Results of the micromagnetic simulations (data points) and the numerical solution of the equation of motion (full black lines) at 250 K and 300 K. The error bars correspond to the uncertainty (standard deviation/ \sqrt{N} with N denoting the number of realizations) on the simulated velocities. The uncertainty on the solution to the equation of motion is negligible. The right side shows the five paths corresponding to the different temperature realizations at $J_c = 0.1 \text{ A } \mu\text{m}^{-2}$, $1 \text{ A } \mu\text{m}^{-2}$ and $4 \text{ A } \mu\text{m}^{-2}$ at 300 K. Reproduced from [150]. CC BY 4.0.

material disorder to arrive at an equation of motion describing a magnetic domain wall moving along a disordered magnetic nanostrip [150]. This equation was validated by direct comparison of its solution with the full micromagnetic simulation data shown in figure 17. The full black lines are obtained from the numerical integration of the equation of motion and show excellent agreement with the micromagnetic model.

It was shown that, instead of the highly nonlinear creep regime found for nonrigid objects, the velocity of narrow domain walls displays a simple linear dependence on the driving force. Interestingly, these results imply that the domain wall can be described by a point particle, while it is argued in [151] that this is not the case for vortex domain walls in wider nanostrips. However, in the absence of thermal fluctuations, the vortex domain wall motion is captured by the 1D-model, which relies on the same assumption. Thus, it remains to be investigated whether vortex domain walls display a linear or nonlinear creep scaling law in the regime of low driving forces.

As the GPU performance improves over time, ever larger simulations become feasible. In recent years, this allowed one to study domain wall motion for longer timescales [150], or in larger thin film geometries [97–99, 152] than was previously attainable. Furthermore, also large three-dimensional structures [153–155] are starting to become computationally tractable. In the first reports on domain wall motion in such extended structures, it was noted that the long-range demagnetizing field plays an increasingly dominant role resulting in flux closure states containing several topological defects, such as vortex cores, which are key to understanding the rich and complex dynamics found in these systems [153, 155].

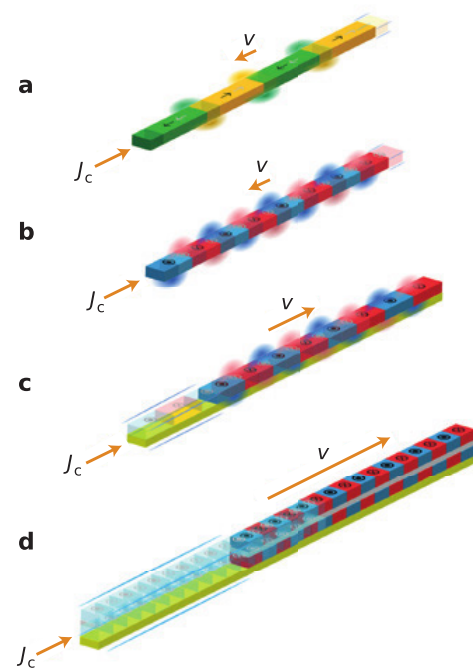


Figure 18. Advancements in the realization of the racetrack memory: (a) Data stored in the magnetization direction of in-plane domains. (b) Data stored in (smaller) domains in PMA nanostrips, in which the domain walls are driven by spin transfer torque. (c) Data driven by chiral spin torques. Realizations (a)–(c) still suffer from large stray fields limiting the data density (shown by shading). (d) Antiferromagnetically coupled nanostrips eliminating these stray fields, and allowing higher domain wall velocities. Reprinted by permission from Macmillan Publishers Ltd: Nature Nanotechnology [157], Copyright 2015.

3.2.8. Domain wall based technological applications. Domain wall motion has been employed in a few technological concepts. In conventional electronics, where only electrical charges are transported, the use of domain walls is rather limited due to the large external fields necessary to move them. However, practical applications exist, e.g. Novotechnik [156] made a spiral-shaped sensor, in which domain walls are generated/annihilated depending on the number of 180 degree turns between the sensor and an external magnet. Because the electrical resistance of the nanostrips discretely changes with the number of domain walls, one can electrically measure the number of rotations of the sensor. This sensor is, for instance, used in combination with a rotation sensor to determine the position of the steering wheel in the automotive industry.

The most promising use of domain wall technology lies in spintronics’ applications (see section 3.5), such as the racetrack memory [158, 159]. In this device, the bits are represented by the magnetization of the domains, see figure 18(a). The position of these bits (domains) can be manipulated by a spin-polarized current to move them over a read or write head. Although high storage densities can be reached by incorporating these nanostrips into 3D structures, there are still physical limits to the data density in these structures, due to the considerable size of the domain walls in these nanostrips, e.g. made of permalloy, the walls are approximately the size of the nanostrip width, which typically is on the order of 100 nm.

Next, stray fields impose a limit on how tight the domain walls can be packed as they are coupled magnetostatically to each other [160]. Some of these limitations are made less stringent in later generations of the racetrack memory concept, as detailed below. Another challenge in the operation of these devices is to control the domain wall positions accurately. To this end, typically, the driving current is applied in pulses, between which the domain walls get pinned to notches [158, 161]. Just as disorder can improve the domain wall mobility above the Walker breakdown, strategically chosen notch locations can also increase the domain wall velocities [162]. Alternatively, zig-zag wires, in which the domain walls can pin to the edges, have been proposed [163]. In later versions, the racetrack memory concept was extended to PMA materials [164] (figure 18, which can accommodate much smaller domain (walls) (b)) and versions which exploited the Dzyaloshinskii–Moriya interaction [157, 165] (figure 18(c)), or even antiferromagnetically coupled nanostrips [166], eliminating stray fields, and thus coupling between domain walls or adjacent nanostrips, (figure 18(d)) to further improve its performance. In PMA materials, notches are not as reliable to pin the domain walls and ratchets with a modulated anisotropy landscape with a sawtooth profile are proposed as a more reliable alternative [167]. Finally, in order to decrease the power consumption of spintronics devices, SOTs can be used instead of STTs to drive the data through the device. Similar to STTs, SOT-based devices only use energy in the active area of the device through which the current flows, but have the additional advantage that significantly lower currents are required to obtain a comparably fast motion [110].

Today, most computations are performed electronically, while most data storage is magnetic. It is possible to make this more homogeneous by performing the calculations, as well as the data storage, magnetically, although it remains to be seen whether such configurations can outperform the current combined approach. Aiming at magnetic computing, another popular use of domain walls in spintronics is domain-wall logic [168–170]. The concept of domain wall logic gates has been proven to work in simulations and in some cases experimentally [168, 171, 172]. In a first implementation, these gates were quite bulky and relied on large external fields to operate [168]. Recently, however, also current-driven domain wall motion based logic gates were presented where the magnetic bits were represented by the direction of the domains [171]. As the functionality of the logic gates might depend on the chirality of the domain wall, methods have been proposed to write this quantity reliably [173, 174]. To further increase the information density of these devices, logical gates have been proposed where the information was stored in the different domain walls [175], and in the future, even smaller ‘walls within walls’ could serve as information carriers [109]. These structures, found in wide PMA nanostrips, do not display a Walker breakdown and thus have the additional advantage of very fast internal wall propagation through larger walls, serving as guides. To add to the versatility of the logic concepts, just like in magnonic applications (see section 3.4), attention has been paid to reconfigurable logic gates [176].

3.3. Skyrmion dynamics and DMI

In chiral magnets, the rotational degeneracy of the exchange energy is lifted due to the Dzyaloshinskii–Moriya interaction, which stabilizes rotations with a certain handedness in the magnetization. The origin of this antisymmetric exchange interaction is already mentioned in section 1.2.4. The importance of the rotation direction is manifested in the terms linear in gradient $\nabla \cdot \mathbf{m}$ in the expression for the DMI energy density given in equation (16). If the DMI is sufficiently strong, chiral magnets can host chiral spin structures such as cycloids (contiguous Néel walls), helices (contiguous Bloch walls), chiral bubble domains, skyrmions, skyrmioniums (skyrmion in a skyrmion), and even more complex combinations. In addition to the stabilization of chiral spin structures, the DMI also has a significant effect on the propagation and dispersion of spin waves.

A bubble domain in a ferromagnetic film with PMA is a circular domain outlined by a single closed domain wall with an in-plane magnetization which is stabilized by dipolar interactions. A skyrmion is also outlined by a single domain wall, but unlike the bubble domain, it is mainly stabilized by the DMI and is much smaller in size. Skyrmions can have diameters in the nanometer range and are protected by a topological barrier. [177] The combination of these two properties makes skyrmions very attractive to the design of a new generation of magnetic memory and logic gates. Recently, a review paper about skyrmions and their potential applications was published [178].

In the remaining part of this section, we focus on micromagnetic simulations of thin ferromagnetic PMA films and an interfacially-induced DMI. These systems are the most promising to serve as a host for isolated skyrmions at room temperature and low applied field, which are necessary prerequisites for the realization of skyrmion-based devices [178]. In general, the magnetization in these system consists out of up and down domains separated by homochiral Néel domain walls.

When performing micromagnetic simulations with DMI, there are at least three computational aspects which should be taken into account: the cell size, issues with topological transitions, and non-trivial boundary conditions. We will touch upon these three aspects before providing a short summary of the more influential micromagnetic simulations of chiral magnets with an interfacially-induced DMI.

In contrast to the exchange interaction, which tends to align the magnetic moments, the DMI favors a rotation over neighboring magnetic moments. A strong DMI (relative to the exchange stiffness) induces spatial variations of magnetization on a small length scale. Hence, besides the two characteristic length scales mentioned in the introduction (equations (12) and (13)), the DMI introduces a third characteristic length scale $2A_{\text{ex}}/D$ [179]. The value for this characteristic length scale lies in the nanometer regime for materials with a strong DMI. This is important to remember when choosing a cell size in micromagnetic simulations. As a rule of thumb, the cell size is small enough if the angle between the magnetic moments of neighboring cells is smaller than 0.4 rad [56].

For the simulations presented further down in this section, cell sizes between 1 nm and 2 nm are used to meet this requirement. If the cell size has to be in the sub nanometer range due to strong local variations of magnetization, one should consider performing atomistic simulations instead.

The creation and the collapse mechanism of skyrmions are essential for the design of skyrmion-based applications. For example, the skyrmion lifetime should be as large as possible, and one should be able to write and delete skyrmions to design functional skyrmion-based devices. During the creation and the collapse of a skyrmion, a Bloch point (two points with opposite magnetization infinitely close together) is unavoidable. This is why a skyrmion is said to be topologically protected [177]. Within the micromagnetic theory, such a Bloch point is a singularity and has an infinite exchange energy density, which makes this transitions unphysical. In micromagnetic simulations, however, these transitions can occur, but the related energies are extremely dependent on the cell size. Therefore, micromagnetic simulations of creation and annihilation of skyrmions, as well as other processes which involve Bloch points, should be avoided. One has to resort to atomistic or multi-scale simulations, in which the nudged elastic band method can be used to accurately describe these transitions and related energy barriers [49, 177, 180–183].

The last computational aspect, regarding simulations of chiral magnets, which we will discuss is the boundary condition. This condition can be derived by minimizing the free energy at the interface. For an ordinary ferromagnet this yields the Neumann boundary condition $\partial \mathbf{m} / \partial \hat{n} = 0$ with \hat{n} the normal of the interface, but it becomes non-trivial when adding DMI [179]⁴:

$$\frac{\partial \mathbf{m}}{\partial \hat{n}} = \frac{D}{2A_{\text{ex}}} \mathbf{m} \times (\hat{e}_z \times \hat{n}). \quad (39)$$

In finite chiral ferromagnetic films, a relaxed magnetic state exhibits a canting of the magnetic moment at the edges. This edge state meets the above boundary condition. Whether this boundary condition should be explicitly implemented is still a topic of ongoing debate. *mumax*³ (version 3.9.2) uses the Neumann Boundary condition given above, whereas OOMMF does not. Relaxed magnetizations of both simulation packages are identical, including the profile of the edge state.

If one studies a single relaxed Néel domain wall in chiral magnetic films analytically, one finds that the domain wall width $\delta_w = \pi \sqrt{A_{\text{ex}} / K_{\text{eff}}}$ is unaffected by the DMI strength. Here, the effective anisotropy K_{eff} includes the uniaxial magnetocrystalline anisotropy K , as well as the shape anisotropy. In contrast to the domain wall width, the energy (per unit wall area) does depend on the DMI strength and reads [179]

$$\sigma_{\text{wall}} = 4\sqrt{A_{\text{ex}} K_{\text{eff}}} - \pi D. \quad (40)$$

From this, we can conclude that the ground state is uniform for DMI strengths lower than the critical DMI strength $D_c = 4\sqrt{A_{\text{ex}} K_{\text{eff}}} / \pi$. For a strong DMI $D > D_c$, a (free)

domain wall yields a negative energy contribution. In this case, the ground state is a cycloid with a decreasing wavelength for an increasing DMI strength. The full phase diagram of stable magnetic states (ground state and excited states) in chiral ferromagnetic films can become very complex [184, 185]. To investigate the numerous stable states with micromagnetic simulations, one could repeatedly relax a random magnetization for a given system and conditions. However, due to the existence of topological barriers, it is more likely to find high energy states with tiny domains than the more smooth low-energy states. This issue can be resolved by using initial magnetizations with a randomness on different length scales. The brute force character of such an investigation makes it only possible on fast GPU codes and demands a fast relaxation of the magnetization. The most efficient way to relax the magnetization is to cancel the precession term in the LLG equation. In addition to this relaxation method, *mumax*³ also offers a conjugate gradient method developed by Exl *et al* [186].

To demonstrate the complexity of the phase diagram of chiral ferromagnetic films, figure 19 depicts all stable magnetic states of small square platelets with a DMI strength $D > D_c$ [185]. The ground state is uniform for thin platelets and otherwise displays a cycloidal state. The number of domain walls in the cycloidal ground state depends on the size of the platelet in such a way that the cycloidal wavelength is approximately equal to the cycloidal wavelength of the ground state in an extended chiral magnetic film. The excited states can become very complex, especially for larger platelets.

From an applications point of view, the most interesting chiral ferromagnetic films have considerable DMI strength, just below the critical DMI strength D_c , since they can host small skyrmions without needing a strong applied field [178]. The ground state of these films is uniform, but it is possible to have an excited state with a single small isolated skyrmion stabilized by the DMI. These isolated skyrmions can be considered as particles which can be moved by means of in-plane spin-polarized currents or vertically injected pure spin currents [187] (see section 1.2.8 for the micromagnetic description of these currents). Analogously to the current-induced domain wall motion discussed in section 3.2, these currents exert a spin transfer torque (SST). This results in a forward motion of the skyrmion along the direction of the current, and a motion perpendicular to the current. The existence of the transverse motion is called the skyrmion Hall effect, which is due to gyrotropic effects related to the topological character of the skyrmion. The equation of motion for the skyrmion's position \mathbf{R} can be derived analytically using the collective coordinate approach of Thiele in which the skyrmion is considered to be a rigid spin structure [68]:

$$\mathbf{F}_{\text{ext}} + \mathcal{G} \times \dot{\mathbf{R}} + \alpha \mathbf{D} \dot{\mathbf{R}} = 0 \quad (41)$$

with \mathcal{D} a constant related to the profile of the skyrmion and $\mathcal{G} \parallel \hat{e}_z$ the gyrovectore causing the skyrmion Hall effect. \mathbf{F}_{ext} is the external force working on the skyrmion coming from, e.g. spin-polarized currents. Thiele's equation yields a good approximation of the motion of a single isolated skyrmion in an extended uniform film and corresponds well with full micromagnetic simulations.

⁴ There is a sign difference in the DMI energy density definition in *mumax*³ and in [179], consequently, there is also a sign difference in the boundary conditions.

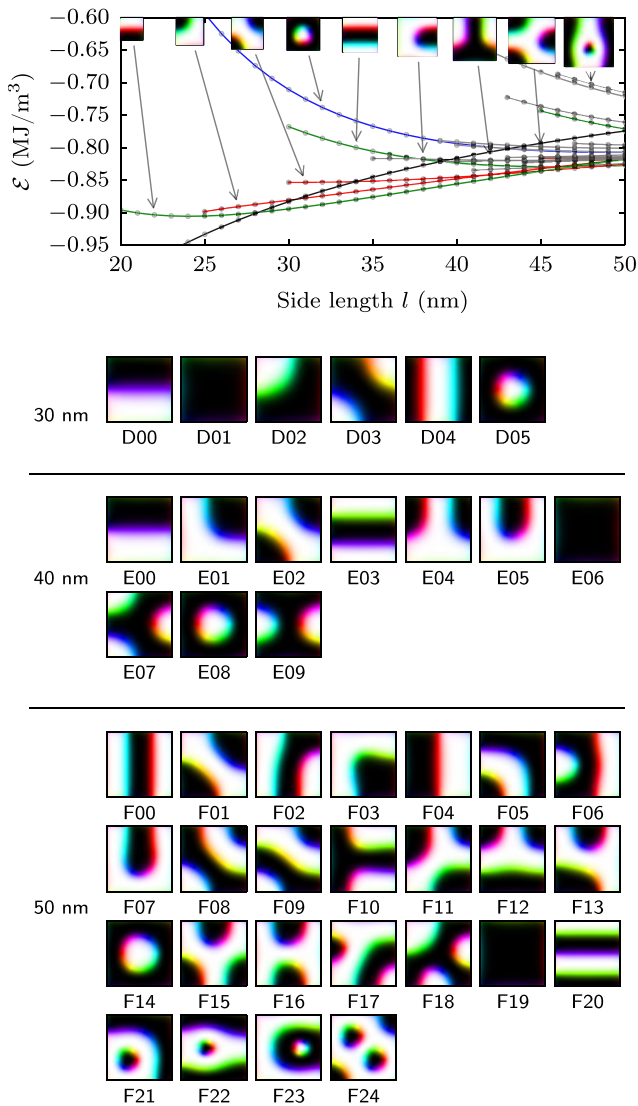


Figure 19. Phase diagram of square platelets with exchange stiffness $A_{\text{ex}} = 15 \text{ pJ m}^{-1}$, an effective uniaxial anisotropy perpendicular to the film $K_{\text{eff}} = 0.8 \text{ MJ m}^{-3}$, DMI strength $D = 5 \text{ mJ m}^{-2} > D_c$ and no applied field. The energies of all stable states are given in the function of the side length l . For the platelets with side length 30 nm, 40 nm, and 50 nm, we show all stable states in order of increasing energy. Reprinted figure with permission from [185], Copyright 2016 by the American Physical Society.

The collective coordinate approach of Thiele is not very useful to describe the motion of a skyrmion in more complex and realistic situations. For example, to study a skyrmion on a skyrmion racetrack, one has to resort to full micromagnetic simulations. A skyrmionic racetrack is a small chiral ferromagnetic strip in which a skyrmion can be moved by applying a spin-polarized current along the strip [16, 188, 190]. The repulsive force between a skyrmion and the boundaries counteracts the skyrmion Hall effect. The skyrmion Hall effect can become too strong for large currents, which will cause the skyrmion to annihilate at the racetrack’s border. For low currents, the repulsive force is strong enough to overcome the skyrmion Hall effect and hold the skyrmion on the racetrack. The results of a simulation of such a functional skyrmion

racetrack are shown in figure 20. Impurities and disorder in the racetrack have a considerable effect on the trajectory of a skyrmion. For example, skyrmions can get pinned at impurities, which lowers the skyrmion velocity and introduces a threshold current [191]. Furthermore, Kim *et al* showed that a disorder potential strongly influences the direction of the skyrmion propagation [192].

To design advanced skyrmionic-based devices, one could not only alter the geometry of the chiral ferromagnetic film, but one could also locally modify the material parameters. Zhang *et al* demonstrated with micromagnetic simulations how one could add a voltage-controlled skyrmion gate on the racetrack [193]. A local electric field can increase the PMA due to charge accumulations, which creates a potential barrier for a skyrmion. Another option is to modify the DMI strength locally by altering or removing the top or bottom heavy metal layer which induces the DMI. In such heterochiral magnetic films, it is possible to have confined chiral spin structures in regions with a strong DMI [194]. A spatially-engineered DMI can be used to create a skyrmion racetrack by confining a skyrmion in a high-DMI strip. Another application of the spatially-engineered DMI is the design of magnetic domains of arbitrary shape and size by confining the domain walls in high-DMI regions (see figure 21).

The DMI stabilizes not only chiral spin structures but also has a profound effect on the propagation of spin waves. This is due to the asymmetric spin-wave dispersion relation [195]. The interaction between spin-waves and chiral structures in the ferromagnetic film with DMI will be briefly discussed in section 3.4.

3.4. Spin-waves and magnonics

Magnonics [196] is an emerging field of magnetism that studies the generation and manipulation of spin waves on the nanoscale, as they hold great potential for next-generation information processing and transmission technologies. In particular, magnetization dynamics naturally occur at frequencies up to tens of terahertz, yet can easily be confined at the nanoscale and converted to electrical signals. Thus, all-metallic magnonic devices are believed to be compatible with, yet superior to, semiconductor technology. Analytical description of such systems is typically limited as magnetostatic effects play a significant role in their behavior. Therefore, micromagnetic simulations play an essential role in the development of magnonic technology.

In fact, GPU-accelerated micromagnetic simulations allow for the understanding of the optical excitation of spin waves in permalloy films with ultrashort laser pulses [197]. They revealed that a rapid demagnetization of the sample, which happens in the area exposed to the focused laser light, creates a broadband pulse of a dipolar field that is highly localized in space. Consequently, spin wave caustic beams get excited with their direction and mean wave-vector set by the magnetization direction and laser spot size, respectively. It is worth mentioning that those were the very first simulations that studied ultrafast and picosecond magnetization dynamics simultaneously in large-scale magnetic structures.

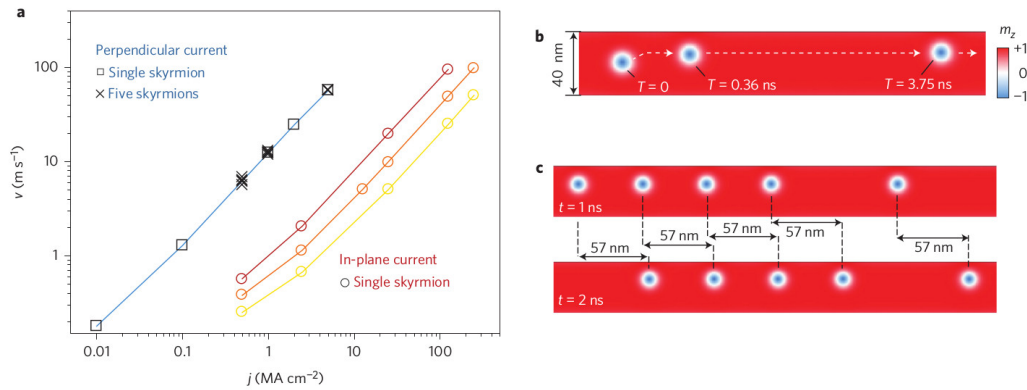


Figure 20. (a) Skyrmion velocity v as a function of current density j for in-plane currents with different values of the non-adiabaticity parameter β (0.15, 0.30 and 0.60 in yellow, orange and brown lines and circles, respectively) and for vertical currents (blue line, squares for isolated skyrmions, crosses for the chain in (c)). (b) Trajectory of a single skyrmion driven by a vertical current ($j = 5 \text{ MA cm}^{-2}$, $v = 57 \text{ m s}^{-1}$). (c) Chain of five skyrmions with two different spacings driven by a vertical current ($j = 5 \text{ MA cm}^{-2}$). The values of $D = 3 \text{ mJ m}^{-2}$ and current polarization $P = 0.4$ were used in these calculations. Reprinted by permission from Macmillan Publishers Ltd: Nature Nanotechnology [188], Copyright 2013.

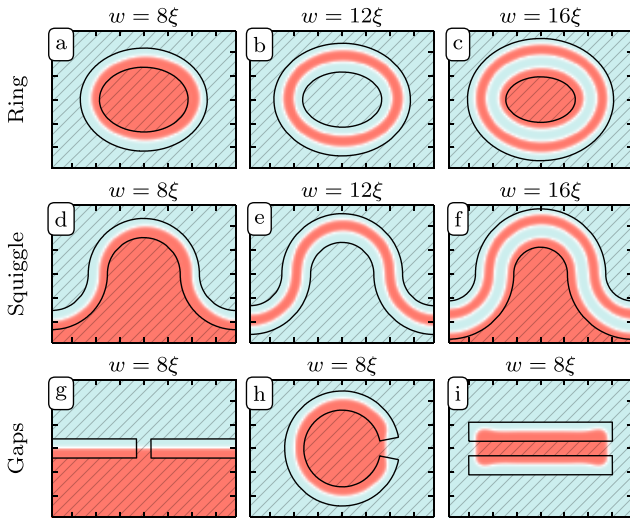


Figure 21. Spatial magnetization profiles of the lowest energy states for high-DMI strips of different shapes and width w (expressed in $\xi = A_{\text{ex}}/K_{\text{eff}}$. The DMI strength is $1.18D_c$ inside the strips (outlined by black lines) and zero elsewhere (shaded area). Reprinted figure with permission from [194], Copyright 2017 by the American Physical Society.

Recently, micromagnetic modeling was also employed to reveal the origin of the asymmetric lineshape in so-called all-metallic pseudo spin valves driven by RF currents injected through the nano-contact [198]. It was demonstrated that, in contrast to the direct current driven case, the microwave Oersted field generated by the nanocontact provides a broadband excitation of the propagating exchange-dominated spin waves. So the spectrum of the generated spin waves is determined by their dispersion relation and the spatial properties of the Oersted field.

For the successful implementation of wave-like computing, which employs phase as the information carrier, it is important to create monochromatic spin wave sources. It has been demonstrated that pinned domain walls, driven by the spin transfer torque provided by the microwave spin polarized current, can excite highly coherent spin waves [199].

Their wavelengths and frequencies can reach 10 nm and 100 GHz, respectively, depending on the domain wall size and frequency of the excitation signal. The authors also demonstrated that control of magneto-crystalline anisotropy would allow one to create highly tunable spin wave sources. Alternatively, one might employ direct pure spin currents to drive the highly localized magnetization auto-oscillations in thin magnetic films and then couple them to the propagating spin waves in adjacent magnetic nanowires [200]. The efficiency of this coupling is subject to the wavelength and frequency matching between the source and the waveguide following the simulated magnonic dispersion relation. These results are beneficial for the development of the spin wave logic devices simulated by Klingler *et al* [201]. Although these authors employed forward volume magnetostatic spin waves, exchange-dominated magnons would enable even higher operational frequencies and would allow downscaling the suggested devices to sub-100 nm length scales.

The development of nanopatterned magnetic media relies on the understanding of transmission and reflection of spin waves at interfaces. Although analytical approaches are more flexible in defining boundary conditions for these problems, they cannot easily deal with highly anisotropic magnonic dispersion relations and the non-uniform internal magnetic field in nanostructures. Thus, micromagnetic simulations were employed to study the angular resolved scattering of the spin waves from the edge of the magnetic material [202]. The Goos-Hänchen effect, a lateral displacement of the reflected beam, was observed depending on the pinning strength at the interface. Also, bending of the spin waves was revealed when the structure was magnetized orthogonally to the edge, consistent with the strongly non-uniform internal field. The effect was later confirmed experimentally and in micromagnetic simulations by testing Snell's law at the interface of two magnetic films of different thicknesses [203]. These findings are a step towards the development of graded refractive index magnonic materials.

Although magnetization dynamics are naturally confined at the nanoscale, the nano-patterning itself might (a) impose

additional losses to the propagating spin waves and (b) would not easily allow for reconfigurable architectures. So Garcia-Sanchez *et al* [204] employed large scale micromagnetic simulations to demonstrate semi-confinement of spin waves by nano-scale domain walls. This was later observed experimentally by Wagner *et al* [205] in 40 nm wide walls. In addition to much reduced extrinsic magnetic losses, such channeled spin waves were found to have a vanishing magnetostatic dispersion leading to higher group velocities and propagation lengths compared to the bulk magnons in the same media. It has also been demonstrated that a pair of such domain-wall-based waveguides could be closely packed on the sub-200 nm scale, yet support interdependent (noninteracting) propagation of channeled spin waves. The experiment also revealed that they could be moved over a distance of several micrometers with a field of only 1 mT. In addition, micromagnetic simulations suggested that there is strong interaction between Néel-type domain walls and incident spin waves in the presence of a Dzyaloshinskii–Moriya interaction [206]. This not only enables manipulation of the spin wave propagation, but might allow one to employ magnons to move domain-wall-based waveguides in all-magnonic re-configurable devices.

Magnonics typically studies quasi-linear magnetization dynamics, but nucleation of nonlinear spin waves might be beneficial to the applications. So, detailed knowledge of magnonic spectra and their nonlinear properties is essential. For instance, it has been predicted micromagnetically that a vortex core polarity could be switched with a nonlinear self-focusing radial spin wave confined in a magnetic nanodisk [207]. Simulations were also extensively used to validate the analytical prediction of the new class of spin wave instabilities that emerge in low magnetic fields, which could be employed for nucleation and synchronization of magnetization dynamics in magnonic devices [208].

GPU-accelerated micromagnetic modeling also enables interdisciplinary studies. For example, it has been experimentally demonstrated, and afterward reproduced in simulations, that anti-dot arrays can be used for biosensing applications [209, 210] as their magnonic resonances experience significant frequency shifts depending on the concentration of magnetic nanoparticles.

3.5. Spintronics and spinorbitronics

Recent advances in spintronics and spinorbitronics allow the nucleation and sustenance of high amplitude magnetization auto-oscillations and even promote switching with direct applied electrical currents. Although this is already employed in commercially available magnetic random access memory (MRAM), gigahertz-band signal generation and, recently, neuromorphic computing with spintronic devices are hot research topics.

Both approaches rely on the ability of spin torque oscillators to synchronize with each other reliably and controllably. This problem has seen rather slow development since the first observation of spin-wave mediated phase locking of a pair of devices in 2005. A breakthrough was made with the help of a GPU-accelerated micromagnetic simulation that allowed one

to optimize the spin wave propagation between oscillators and achieve synchronization of up to five oscillators separated by as far as 1 μm [211]. As emitted magnons are highly directional due to the Oersted field produced by the nanocontact, one needs to make sure that oscillators are placed along the spin wave propagation direction. Finally, in contrast to earlier assumptions, simulations revealed that the synchronization has a driven character.

Shortly after, a mutual synchronization of up to nine spin-orbitronic oscillators in strong oblique magnetic fields has been experimentally demonstrated [212]. The modeling suggested that, in contrast to the nanocontact spin torque oscillators, the magnetization auto-oscillations are strongly localized. So the phase locking is mediated by the mutual direct exchange and dipolar interactions that increase with the applied current due to the mode expansion. If the magnetic bridge connecting such devices is engineered to enhance the expansion, then long range synchronization is achieved in the devices separated by 4 μm . Subsequent simulations suggested that auto-oscillations emerge from the magnonic edge modes and their expansion properties strongly depend on the strength and out-of-plane angle of the applied magnetic field [213].

Large-scale mumax³ micromagnetic simulations paired with the Kuramoto model enabled the study of complex synchronization patterns in arrays of vortex spin torque nano-oscillators [214]. It was found that the critical coupling strength needed to synchronize the entire array scales as $\log(N)$, where N is the number of oscillators. So for realistic values of the coupling, only local synchronization is possible in such systems. The existence of such synchronization domains gives rise to the nucleation of topological defects in the phase field.

Overall, it is quite common to study current-driven magnetization auto-oscillations with micromagnetic simulations. This is typically done by reproducing the corresponding experimental data. In particular, micromagnetic simulation revealed the fine structure of weakly localized magnetization dynamics in spin-current nano-oscillators based on nonlocal spin injection [215]. Modeling also validated a multi-mode spin torque oscillator model that explained mode coexistence and hopping in nanocontact oscillators [216]. It has also been revealed that such devices can support solitons with p-like symmetry [217]. Furthermore, excitation of large spin wave bullets by the pure spin current injection in insulating Yttrium Iron Garnet has been confirmed [218], which opens new possibilities for the development of spintronic devices with lower power consumption. More recently, micromagnetic simulations were used to explain the non-monotonic frequency versus current tunability of the 20 nm width constriction-based spin Hall nano-oscillator [219].

Micromagnetic simulations are also a driver in the research of magnetic droplets, which naturally appear in spintronic devices with a PMA free layer. In particular, modeling suggested that droplets can exist in low-dimensional magnetic structures, e.g. wires [220]. Later, drift resonances of the droplets were understood, suggesting their stability at room temperatures [221, 222]. Also, fusion and fission of droplets [223] and their phase locking [224] were demonstrated

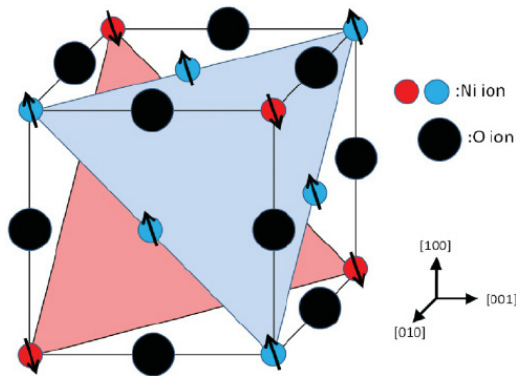


Figure 22. Antiferromagnetic ordering in NiO and CoO. The spins belonging to the same AFM sublattice are drawn in the same color. The (1 1 1) planes are uncompensated and (100) planes are compensated. Reprinted figure with permission from [229], Copyright 2012 by the American Physical Society.

micromagnetically. Finally, transport properties of the droplets were recently studied by Loreto *et al* [225], who suggested that they can be used in racetrack memory since they do not experience a skyrmion Hall effect.

Modeling also has predictive power. For instance, nucleation of the dynamical magnetic skyrmion in the absence of a Dzyaloshinskii–Moriya interaction has recently been predicted, and the interaction with magnetic droplets and the transition to static skyrmions were studied [226]. Furthermore, a design of the skyrmion-based spin torque oscillator that could potentially operate at much smaller current densities than the typical spin torque nano-oscillators has been suggested [227]. Modeling also suggested that magnetic skyrmions can be reliably nucleated in contact-based spin Hall nano-oscillators [228].

3.6. Exchange bias

Exchange bias occurs when a ferromagnetic (FM)/antiferromagnetic (AFM) bilayer is cooled in an external field below the Néel temperature. It was first discovered by Meiklejohn and Bean [39] in 1956. Considering the spin orientation in AFM monoxides such as NiO and CoO, one can see (figure 22) that compensated as well as uncompensated crystallographic planes can be present at the FM/AFM interface. At a compensated interface (e.g. the (100) plane in NiO), both AFM sublattices couple equally to the ferromagnet, whereas for an uncompensated interface (e.g. the (1 1 1) plane in NiO), only one AFM sublattice interacts with the FM layer.

The presence of frozen uncompensated AFM spins at the interface induces a unidirectional shift of the hysteresis loop. This shift generally is antiparallel to the field cooling direction (*negative exchange bias*) both in the case of a parallel as well as an antiparallel interfacial coupling. Antiferromagnetic spins, which are strongly coupled to the FM layer or have a low anisotropy, rotate together with the FM and lead to an enhanced coercivity [230].

In the case of a compensated AFM interface, the magnetic system will try to minimize its total energy by canting both AFM sublattices towards the magnetization direction in the

FM. This second order magnetic interaction, called spin flop coupling [231, 232], induces an enhanced coercivity perpendicular to the anisotropy axis of the AFM, but does not lead to a shifted hysteresis loop [233, 234].

The pinning of a ferromagnetic layer through exchange bias, and the FM/AFM interfacial coupling in general, have some important technological applications such as GMR or TMR spin valves, which are used in reading heads and MRAM devices. Exchange bias can also provide a way to beat the superparamagnetic limit [235] and spin flop coupling can lead to a lower switching field in nanomagnets [236]. Interestingly, in 2015 Fukami *et al* [237] have shown that an exchange biased Co/Ni multilayer with an out-of-plane magnetization can be switched by applying a current in the AFM layer and by making use of a spin orbit torque. The presence of an in-plane exchange bias field in the direction of the current eliminates the necessity to apply an external field on the multilayer to achieve deterministic switching of the ferromagnet [238, 239].

3.6.1. Modeling of exchange bias. To model exchange bias, one usually resorts to simple analytical models [230, 240, 241] as these can give some indications about the dependency of these phenomena on the physical parameters. Although these models can capture the essential physics of a magnetic system in most cases, it is not a very realistic approach when dealing with real interfaces in, typically, polycrystalline antiferromagnets. Also, systems in which the magnetostatic field of the FM plays an important role cannot or can hardly be described in these models due to the complex nature of the demagnetization energy.

Alternatively, one can consider every individual spin on the atomic level (e.g. the Vampire [242] software package). Due to the smallness of the lattice constant however, these calculations require a lot of computational resources as many lattice points are needed to be taken into account and so only small magnetic structures can be studied without making use of supercomputers.

In order to study static effects due to the interfacial coupling between a ferromagnet and an antiferromagnet, it is not necessary to model the AFM on an atomic scale and a micromagnetic approach can be very valuable as an intermediate approach between limited theoretical models and the full atomistic description of an antiferromagnet.

Recently, it was shown how the mumax³ framework [56] can be used to model compensated [234], uncompensated [243] and mixed [234] antiferromagnetic interfaces. It was demonstrated that phenomena such as exchange bias, spin flop coupling and athermal training can be taken into account by using an effective micromagnetic approach, thus providing a realistic description of static effects due to the interfacial coupling between a FM and an AFM.

3.6.2. Modeling of uncompensated antiferromagnetic interfaces. When considering a FM coupled to an uncompensated AFM interface, the AFM can be modeled as a single pseudo-ferromagnetic layer [234, 243] to which one can attribute some effective parameters, e.g. an anisotropy constant and a positive

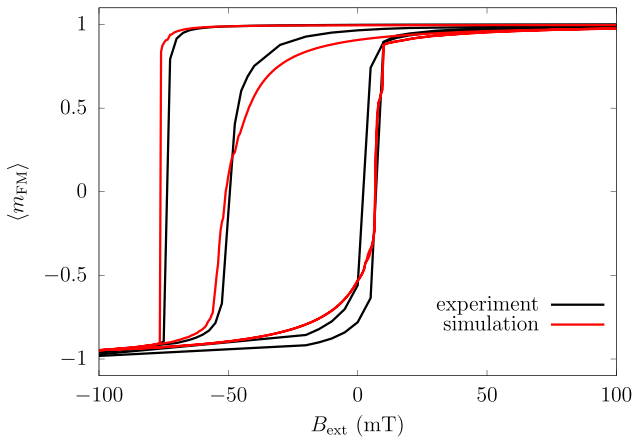


Figure 23. Comparison of the simulated hysteresis loop (red) with the experimental data of a Co(30nm)/CoO(3nm) bilayer [244] (black). The external field was applied along the field cooling direction. Reproduced from [243]. © IOP Publishing Ltd. All rights reserved.

intralayer exchange stiffness. By dividing the AFM layer into several grains [123], one can locally vary the coupling constant between the FM and the AFM, the anisotropy constant and the anisotropy axis of an AFM grain. Also, the presence of a planar domain wall in the antiferromagnet, as described in the model of Mauri [240], can easily be taken into account. Further details on the exact implementation of an uncompensated AFM interface in mumax³ can be found in [234].

Using this approach, one can reproduce experimental data, e.g. athermal training in an exchange biased Co(30nm)/CoO(3nm) bilayer [244], as shown in figure 23. A good quantitative agreement is found between the simulations [243] and the experimental data [244]. Approximately 30% of the AFM grains were pinned in the field cooling direction, inducing exchange bias, and 70% of the AFM grains were considered to be rotatable, leading to an enhanced coercivity. Also, the asymmetry between the descending branch and the ascending branch of the first hysteresis loop, which is a typical feature of athermal training, can be reproduced as well as the reduction in coercivity and bias field.

Using the same Co/CoO system, it was also confirmed [243] that a trained hysteresis loop can be reinitialized to an apparent field cooled state by applying an external field, perpendicular to the field cooling direction [245, 246] and that there can be a difference in the reversal mechanism between the descending and the ascending branch of the first hysteresis loop [247]. The latter is illustrated in figure 24. Starting from a field cooled state (figure 24(a)), the first reversal of the Co layer towards negative saturation happens through the formation of magnetic domains in the FM and corresponding domains in the AFM, as is shown in figure 24(b). When returning to positive saturation, however, the reversal of the FM now happens through coherent rotation of these domains. This is also the case in all subsequent hysteresis loops (descending as well as ascending branches), as can be seen in figure 24(c). The asymmetry in the reversal mechanism has been experimentally observed in Co/CoO bilayers by using polarized neutron reflectometry [247].

This micromagnetic model of an uncompensated AFM interface can also be used to study *positive exchange bias*. In the case of high cooling fields, the hysteresis loop is sometimes shifted in the same direction as the cooling field [248–251]. This is often explained by considering an antiparallel interfacial coupling between the FM and the AFM layer and by taking into account the Zeeman energy of the AFM during field cooling. A similar model like the one proposed by Kiwi [248] for compensated surfaces can also be applied to uncompensated AFM interfaces. When assuming that the cooling field H_{cf} is oriented along the uniaxial anisotropy axis \mathbf{u}_{AFM} of the AFM and that the ferromagnet is saturated in the same direction as the cooling field, the total surface energy density of this system can be written as

$$\sigma = J_{\text{I}} \mathbf{m}_{\text{FM}} \cdot \mathbf{m}_{\text{AFM}} - K_{\text{AFM}} t_{\text{AFM}} (\mathbf{u}_{\text{AFM}} \cdot \mathbf{m}_{\text{AFM}})^2 - \mu_0 M_{\text{AFM}} t_{\text{AFM}} \mathbf{m}_{\text{AFM}} \cdot \mathbf{H}_{\text{cf}} \quad (42)$$

where t_{AFM} and M_{AFM} are the thickness and the sublattice saturation magnetization of the uncompensated AFM, respectively. The first term is the exchange coupling between the FM and the uncompensated AFM layer, the second term is the uniaxial anisotropy energy of the AFM, and the last term represents the Zeeman energy of the uncompensated AFM in the cooling field H_{cf} . Constant energy contributions were omitted, and we have assumed an antiparallel coupling between the FM and the AFM for a coupling constant $J_{\text{I}} > 0$. Examining the stability conditions, one can show that pinned AFM spins will lead to a positive exchange bias in this model if

$$\mu_0 H_{\text{cf}} \geq \frac{J_{\text{I}} + 2K_{\text{AFM}} t_{\text{AFM}}}{M_{\text{AFM}} t_{\text{AFM}}} \quad (43)$$

At this threshold value, the Zeeman energy of the uncompensated AFM during field cooling is strong enough to overcome the anisotropy energy and the interfacial coupling between the AFM and the FM, assuming the AFM was initially located in its global energy minimum, i.e. in an antiparallel state with respect to the saturated ferromagnetic layer. Cooling fields which satisfy equation (43) will switch the AFM grain towards an orientation parallel with the FM, corresponding to a local energy minimum due to the presence of the uniaxial anisotropy of the AFM. As the AFM spins hardly couple to the external field anymore after field cooling, these spins will stay pinned in this parallel orientation, even during a field sweep. In the case of a uniform uniaxial antiferromagnet, the threshold value for the cooling field leads to a stepwise function for the bias field B_{eb} , jumping from $-|B_{\text{eb}}|$ to $|B_{\text{eb}}|$.

To illustrate the case of positive exchange bias, one can consider a 10nm thick antiferromagnet (grain size of 12nm and sublattice saturation magnetization $M_{\text{AFM}} = 400 \text{ kA m}^{-1}$), coupled to an isotropic permalloy layer ($M_{\text{FM}} = 800 \text{ kA m}^{-1}$ and $A_{\text{FM}} = 1.3 \times 10^{-11} \text{ J m}^{-1}$) of equal thickness. The AFM layer has a uniaxial magnetocrystalline anisotropy, and to make the system more realistic, the anisotropy constants of the grains as well as the interfacial coupling parameters J_{I} of the grains with the FM layer were varied. The value of the anisotropy constant K_{AFM} was randomly distributed between 0 and $2 \times 10^5 \text{ J m}^{-3}$ and likewise the value of J_{I} was

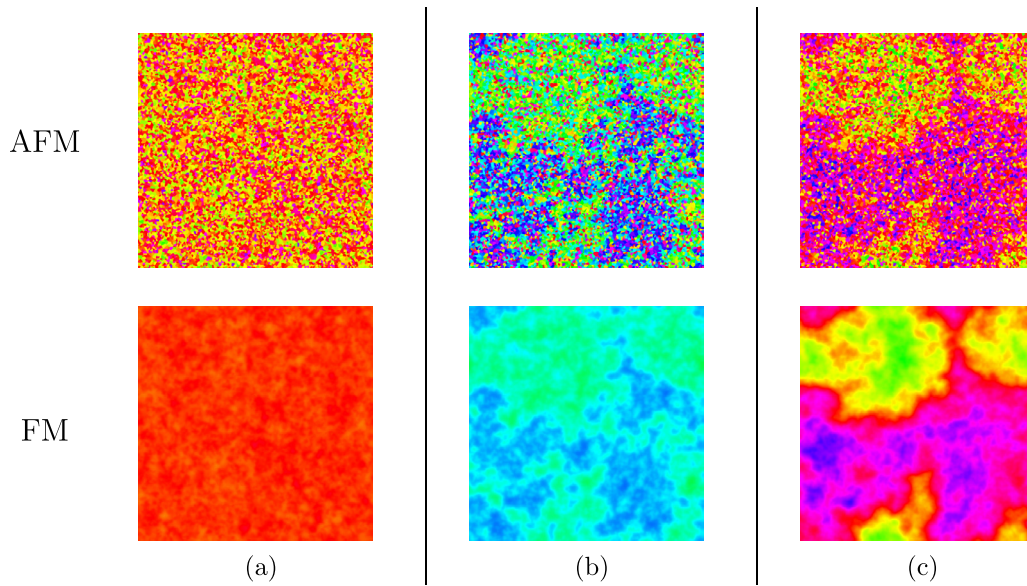


Figure 24. Magnetization of the AFM (top row) and corresponding FM (bottom row) layer at different places in the simulated hysteresis loop. (a) Initial field cooled state. (b) At negative saturation in the first hysteresis loop. (c) In the descending branch of the second hysteresis loop. The reversal in the descending branch of the first hysteresis loop (see figure (b)) happens through domain formation. Further reversals happen through coherent rotation of these domains, as can be seen in figure (c). Reproduced from [243]. © IOP Publishing Ltd. All rights reserved.

randomly distributed between 0 and 2 mJ m⁻², assuming an antiparallel coupling towards the ferromagnet.

The cooling field H_{cf} was applied parallel to the anisotropy axis of the AFM, the ferromagnet was always kept saturated in the field cooling direction, and all AFM grains were initialized antiparallel to the FM, corresponding to the global energy minimum when no cooling field is present. Starting from this state, the antiferromagnet was relaxed in the cooling field. Afterwards, the cooling field was removed, and the system was relaxed again. Depending on the magnitude of H_{cf} , some pinned AFM grains will have made an irreversible transition from the antiparallel state with respect to the FM towards a parallel orientation, inducing positive exchange bias.

The evolution of the bias field B_{eb} as a function of the magnitude of the cooling field $\mu_0 H_{cf}$ is shown in figure 25 (red). One can see that, in accordance to experimental data [251], the bias field is negative for low cooling fields but becomes positive at high cooling fields, even obtaining $B_{eb} \approx 0$ mT when as many AFM grains are oriented parallel as antiparallel to the FM. When the cooling field is large enough to switch all pinned uncompensated AFM grains towards a parallel orientation with the FM, the curve will saturate. One can show (equation (43)) that, for this system, saturation occurs at $\mu_0 H_{cf} = \frac{3K_{AFM,max}}{M_{AFM}} = 1.5$ T with $K_{AFM,max} = 2 \times 10^5$ J m⁻³ the maximal value of the uniaxial AFM anisotropy constant. Also, the case of a polycrystalline AFM, consisting of grains with a uniaxial anisotropy, is shown in figure 25 (green). At saturation, the bias field is reduced by approximately a factor $\frac{2}{\pi}$ due to the random distribution of the magnetization of the pinned AFM grains in the direction of the cooling field. The exact shape of these curves depends on the distribution of the coupling parameter J_1 and the anisotropy constant K_{AFM} in the AFM.

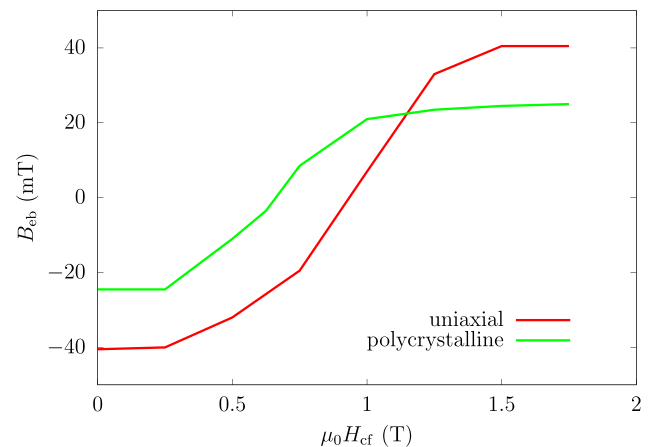


Figure 25. Bias field B_{eb} as a function of the cooling field $\mu_0 H_{cf}$ in the case of a uniaxial (red) or polycrystalline (green) uncompensated AFM. For large cooling fields, the bias field becomes positive.

3.6.3. Modeling of compensated and mixed antiferromagnetic interfaces. At the micromagnetic scale, the two AFM sublattices can be considered as two coinciding, antiferromagnetically coupled, pseudo-ferromagnetic layers [234]. *mumax3* allows only one magnetization vector per cell. Therefore, the two sublattices are separated into two different layers, indicated by AFM₁ and AFM₂ in figure 26. Considering static effects, this separation in space has no physical implications as both layers behave as if they would coincide. The AFM₁ layer, which is not directly adjacent to the FM layer, can be coupled to the FM by adding a custom field and energy term [234]. The negative interlayer exchange stiffness A_{AFM} between the two AFM layers takes into account the nearest neighbor interaction between two antiparallel spins and the positive intra-layer exchange stiffness A_A ensures a correct AFM domain

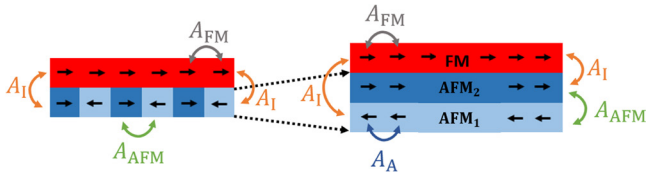


Figure 26. In the micromagnetic approach, an atomic compensated AFM interface (left) is replaced by two continuous AFM layers (right), which are coupled by a negative exchange stiffness A_{AFM} . The FM layer (red) is directly coupled to both AFM₁ and AFM₂ by an interlayer exchange stiffness A_I . A positive intralayer exchange stiffness A_A ensures the correct AFM domain wall energy. Reproduced from [234]. © IOP Publishing Ltd. All rights reserved.

wall energy and can also include the next nearest neighbor interaction. Also mixed (compensated as well as uncompensated) AFM interfaces can be implemented in *mumax*³.

This micromagnetic model of a compensated AFM interface can reproduce experimental data, e.g. spin flop coupling in $\text{La}_{0.7}\text{Sr}_{0.3}\text{MnO}_3/\text{LaFeO}_3$ nanosquares [252]. Besides the usual Landau state, also z-type domain configurations were found in the experiment. Starting from a random state in the FM and semi-random in the AFM, the authors [234] could reproduce both states using this two layer approach.

Hoffmann [253] has shown that antiferromagnets, with a symmetry higher than uniaxial anisotropy, can be in a non-collinear state after field cooling. During the first reversal of the FM, the AFM sublattices relax towards an antiparallel state, inducing athermal training and thus exchange bias in the first hysteresis loop. Using the micromagnetic model [234] of a compensated AFM interface, one can easily investigate these systems.

Figure 27 shows the difference in coercivity between the first and the second hysteresis loop as a function of the biaxial AFM anisotropy constant $k_{b,AFM}$ and the interfacial coupling parameter j_i . Two regions can be discriminated in the phase diagram. The athermal training in the middle region results from Hoffmann training: the two non collinear AFM sublattices relax from the 90° canted state towards an antiparallel orientation after the first reversal of the ferromagnet. The reduction in coercivity in the lower right region of the phase diagram is due to a spin flip transition of the sublattices. However, both regions lead to the typical asymmetry between the descending branch and the ascending branch in the first hysteresis loop.

As biaxial anisotropy is not natively implemented in *mumax*³, a custom effective field and energy density term were added to the input script. This feature gives the user complete freedom to define his/her custom energy contributions. An example of how such a term can be added to a *mumax*³ input file can be found in [234].

3.6.4. Limitations of the micromagnetic exchange bias model. Due to the micromagnetic description of an antiferromagnet and its implementation in *mumax*³, only static effects such as exchange bias, spin flop coupling, and athermal training can be modeled, as these do not rely on the correct dynamical description of the magnetization in the AFM sublattices.

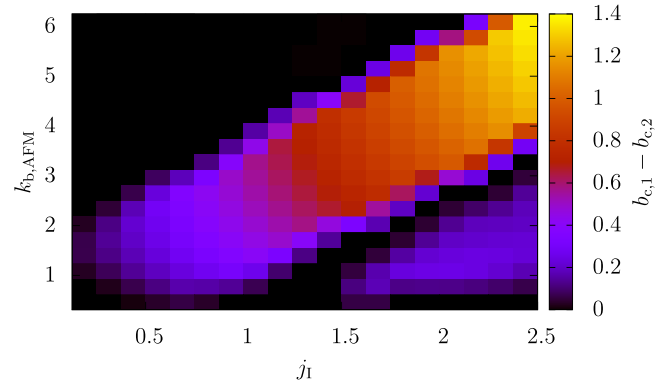


Figure 27. Phase diagram of Hoffmann training for a uniform biaxial antiferromagnet, as a function of the reduced anisotropy constant $k_{b,AFM}$ and the reduced exchange coupling j_i . The color scale represents the difference in coercivity b_c (in reduced units) between the first and second hysteresis loop. Reproduced from [234]. © IOP Publishing Ltd. All rights reserved.

3.7. Artificial spin ices

The complex behavior of magnetic systems is driven by the interplay of multiple interactions. While these interactions often give rise to a single ground state, in some systems, they are at odds with each other, leading to the inability of the system to minimize all its competing interactions: a property called frustration. Frustrated systems contain a large number of degenerate ground states [254] and a considerable amount of ground state entropy [255]. In magnetic systems, it was originally thought necessary to have an antiferromagnetic coupling to induce frustration. Surprisingly, also ferromagnetic couplings can lead to frustration in certain geometries, called spin ices. This is an interesting class of materials where novel physics appear [256], but, unfortunately, it is hard to study as the frustrated interactions are on the atomic length scale. The field only took flight when it was shown that a lithographically fabricated 2D grid of single domain nanomagnets displays the same properties as in naturally occurring pyrochlore spin ices [257]. Such artificial spin ices provide a far more accessible model system in which the interaction details can be tuned at will, e.g. by varying the inter-island distances.

The experimental accessibility of artificial spin ices has sparked much research interest and has led to new approaches to studying frustrated systems. On the one hand, a network theory approach is used to investigate the properties of the complete lattice, e.g. which states can transform into which others [258]. On the other hand, the local excitations within the system are the subject of study [259]. These local excitations are small clusters of nano-islands in which the magnetic moments are reversed, so the configuration contains more energy than a ground state.

A topic of great interest is the dynamics of these local structures. Commonly, these dynamics have to be induced with the help of external excitations [256]. A typical experiment consists of applying an external field to (a previously fully magnetized) spin ice and observing when and how the magnetization reversal takes place [258]. In theory, this is

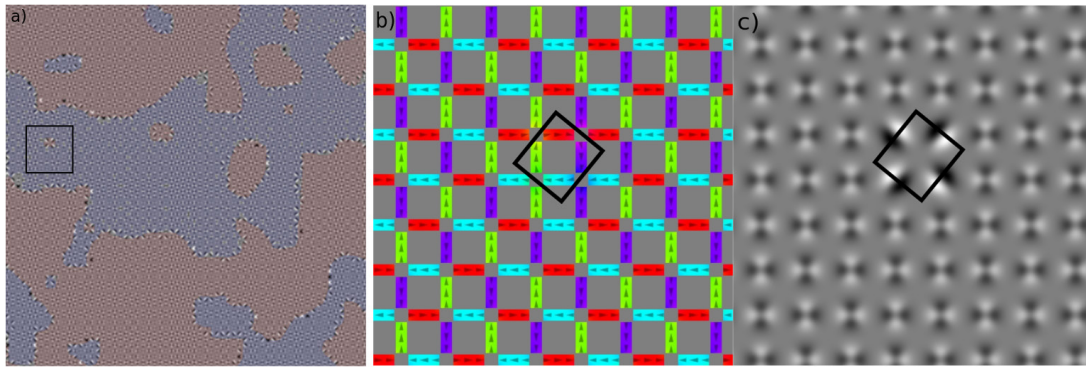


Figure 28. (a) Artificially colored simulated MFM image of an array of 64 by 64 vertices in thermal equilibrium. The red and blue regions are the different ground state configurations. The indicated region is enlarged in panels (b) and (c), and shows the magnetization state (b) of the background with a local excitation on top of it, while (c) depicts a close-up of the simulated MFM image.

a well-defined process in which the system only accesses a few intermediate states. In reality, however, the importance of disorder in spin ice dynamics is not to be underestimated. Even a small amount of disorder, inherently present due to the nature of the sample fabrication, increases the number of available reversal paths by order of magnitude and leads to critical phenomena and avalanches [258, 260]. Recently, the impact of the disorder on the vertex level was also studied [261]. Surprisingly, the defect site in a square lattice enhances flipping of the neighboring sites, while in a Kagome lattice, a defect site breaks the local frustration of the neighboring sites and inhibits them from flipping [261]. The final barrier that had to be overcome to investigate local excitations accurately was to make thermally active samples [262, 263], so external fields are no longer necessary to induce dynamics. This means that the size of the islands, their separation and the magnetic properties of the materials are tuned in such a way that the energy barrier for a single flip of an island is sufficiently low and can be caused by the thermal fluctuations [262]. Only in thermal equilibrium will the system reach the ground state and that we are able to observe the dynamics of the local excitations [254].

It is mainly in these (thermally) excited samples that it becomes worthwhile to use micromagnetic simulations as compared to higher-level models, which reduce the individual nano-islands to macrospins. These macrospin models do not take into account the fact that the intra-island magnetization is not necessarily uniform [264], or even display dynamics in the form of normal modes [265], which can influence the global dynamics of the spin-ice. More detailed studies about the local modes can be found in section 3.4. Whereas micromagnetic simulations used to be quite limited to relatively small geometries, an initial study shown in figure 28 illustrates that it has become feasible to simulate structures with a size of the same order of magnitude as in experimental samples.

Roughly simultaneous with the first realizations of artificial spin ices, it was shown that the ice rules also apply to connected magnetic networks [266]. Here, the system consists of a network of connected uniformly magnetized nanostrips, interacting at the vertices [267]. Reversing the magnetization of a single element is achieved by moving a domain wall, carrying the magnetic charge, through the strip. Compared to the

island lattices where the switching is between binary states and the charge flips from between the vertices, the mobility of the magnetic charges is considerably higher [268]. The second advantage of connected lattices compared to unconnected islands is that the effect of inherent sample disorder is lower in the connected systems [269]. This increases the controllability of the dynamics, while still maintaining the positive effects of the disorder. Similarly, as for unconnected islands, next to honeycomb lattices [270, 271], also other topologies, like brickwork lattices [272], show interesting behavior.

As shown in section 3.2, domain wall motion depends on the internal structure of the domain walls. For instance, the path a domain wall will take at a vertex depends on the walls' polarity and chirality [270]. To correctly simulate this, it is necessary to perform micromagnetic simulations which consider the detailed magnetization of the elements. To date, however, the large computational cost has prevented large scale simulations, and only single vertices [273], or relatively small networks containing only a few vertices have been simulated [270]. However, similar to the unconnected spin ices shown in figure 28, a trend is seen that the newest GPUs allow one to simulate increasingly large structures, which will lead to larger-scale studies that can help to complement experiments.

3.8. Novel micromagnetic approaches

As we mentioned before, micromagnetic simulations based on the LLG model extended with spin transfer torque and thermal stochastic field terms are predominantly used to investigate problems of modern nanomagnetism. Nevertheless, as the technology moves forward we can now access magnetization dynamics on even shorter (femtosecond) timescales, where not only is the magnetization length not conserved anymore, but magnon–electron and magnon–phonon interactions show their distinct characters. It has been demonstrated that these phenomena could be addressed with the Baryakhtar phenomenological model, and the corresponding GPU-accelerated micromagnetic solver, the so-called hotspin, was developed [66]. In fact, it has already been used to reproduce the experimentally observed optical excitation of spin waves [197].

The model also predicts that the magnetic damping constant is not scalar, but a tensor that follows the crystallographic symmetry. Micromagnetic simulations revealed that this should manifest itself in an anisotropic linewidth of magnonic resonances, but the ellipticity of the magnetization precession should be carefully taken into account [274].

Finally, the Baryakhtar model postulates the existence of the so-called non-local magnetic damping, which has been later revealed experimentally as (a) a mode- and size-dependent contribution to the magnonic linewidth in magnetic nano-elements [275] and (b) a reduction of the domain wall mobility [276]. A comprehensive micromagnetic study of this phenomena was then reported by Wang *et al* [277].




4. Conclusions

In this review, we have shown how micromagnetic modeling has evolved in the last decade and took advantage of the capabilities offered by the availability of GPU acceleration. The huge increase in computational power has enabled extensive studies in all fields of magnetism and enabled the simulation of more complex and realistic magnetic systems, and consequently achieved better agreement with experimental studies. As the hardware capabilities of GPUs are still growing and the development of micromagnetic software is continuing, the importance of simulations in magnetism research will increase in the near future.

Acknowledgment

This work was supported by the Fonds Wetenschappelijk Onderzoek (FWO-Vlaanderen) through Project No. G098917N. JL is supported by the Ghent University Special Research Fund (BOF postdoctoral fellowship). We gratefully acknowledge the support of the NVIDIA Corporation with the donation of a Titan Xp GPU used for this research.

ORCID iDs

J Leliaert  <https://orcid.org/0000-0001-8778-3092>
 J De Clercq  <https://orcid.org/0000-0001-7224-853X>
 B Van Waeyenberge  <https://orcid.org/0000-0001-7523-1661>

References

[1] Brown W F 1963 *Micromagnetics* (New York: Interscience)
 [2] Weiss P 1907 *J. Phys. Théor. Appl.* **6** 661–90
 [3] Langevin P 1905 *Ann. Chim. Phys.* **5** 70–127
 [4] Heisenberg W 1928 *Z. Phys.* **49** 619–36
 [5] Barkhausen H 1919 *Physica Z* **20** 401
 [6] Bitter F 1931 *Phys. Rev.* **38** 1903–5
 [7] Sixtus K J and Tonks L 1931 *Phys. Rev.* **37** 930–58
 [8] Bloch F 1932 *Z. Phys.* **74** 295–335
 [9] Landau L and Lifshitz E 1935 *Phys. Z. Sowietunion* **8** 153
 [10] Döring W 1948 *Z. Naturforsch. A* **3** 373
 [11] Gilbert T 2004 *IEEE Trans. Magn.* **40** 3443–9
 [12] Schryer N L and Walker L R 1974 *J. Appl. Phys.* **45** 5406–21
 [13] Lopez-Diaz L *et al* 2012 *J. Phys. D: Appl. Phys.* **45** 323001

[14] Vansteenkiste A and Van de Wiele B 2011 *J. Magn. Magn. Mater.* **323** 2585–91
 [15] Moriya T 1960 *Phys. Rev.* **120** 91–8
 [16] Fert A, Cros V and Sampaio J 2013 *Nat. Nanotechnol.* **8** 152–6
 [17] Nagaosa N and Tokura Y 2013 *Nat. Nanotechnol.* **8** 899–911
 [18] Coey J M D 2010 *Magnetism and Magnetic Materials* (New York: Cambridge University Press)
 [19] Brown W F 1959 *J. Appl. Phys.* **30** S130–2
 [20] Brown W F 1963 *Phys. Rev.* **130** 1677–86
 [21] Lyberatos A, Berkov D and Chantrell R W 1993 *J. Phys.: Condens. Matter* **5** 8911
 [22] Mayergoyz I, Bertotti G and Serpico C 2011 *J. Appl. Phys.* **109** 07D312
 [23] Mayergoyz I, Bertotti G, Serpico C, Liu Z and Lee A 2012 *J. Appl. Phys.* **111** 07D501
 [24] Bertotti G, Serpico C and Mayergoyz I D 2013 *Phys. Rev. Lett.* **110** 147205
 [25] Lee A, Liu Z, Bertotti G, Serpico C and Mayergoyz I 2014 *Physica B* **435** 100–4
 [26] Garanin D A 1997 *Phys. Rev. B* **55** 3050–7
 [27] Baryakhtar V 1984 *Zh. Eksp. Teor. Fiz.* **87** 1501–8
 [28] Hamann H F, Martin Y C and Wickramasinghe H K 2004 *Appl. Phys. Lett.* **84** 810–2
 [29] Schieback C, Hinzke D, Kläui M, Nowak U and Nielaba P 2009 *Phys. Rev. B* **80** 214403
 [30] Berger L 1978 *J. Appl. Phys.* **49** 2156–61
 [31] Berger L 1996 *Phys. Rev. B* **54** 9353–8
 [32] Slonczewski J 1996 *J. Magn. Magn. Mater.* **159** L1–7
 [33] Xiao J, Zangwill A and Stiles M D 2004 *Phys. Rev. B* **70** 172405
 [34] Zhang S and Li Z 2004 *Phys. Rev. Lett.* **93** 127204
 [35] Brataas A, Kent A D and Ohno H 2012 *Nat. Mater.* **11** 372–81
 [36] Sinova J, Culcer D, Niu Q, Sinitsyn N A, Jungwirth T and MacDonald A H 2004 *Phys. Rev. Lett.* **92** 126603
 [37] Liu L, Pai C F, Li Y, Tseng H W, Ralph D C and Buhrman R A 2012 *Science* **336** 555–8
 [38] Mihai Miron I, Gaudin G, Auffret S, Rodmacq B, Schuhl A, Pizzini S, Vogel J and Gambardella P 2010 *Nat. Mater.* **9** 230
 [39] Meiklejohn W H and Bean C P 1956 *Phys. Rev.* **102** 1413–4
 [40] Nogués J and Schuller I K 1999 *J. Magn. Magn. Mater.* **192** 203–32
 [41] Van Pamel A, Sha G, Rokhlin S I and Lowe M J S 2017 *Proc. R. Soc. A* **473**
 [42] Donahue M and Porter D 2004 *Physica B* **343** 177–83
 [43] Newell A J, Williams W and Dunlop D J 1993 *J. Geophys. Res.* **98** 9551–5
 [44] Abert C, Selke G, Krüger B and Drews A 2012 *IEEE Trans. Magn.* **48** 1105–9
 [45] Fu S, Cui W, Hu M, Chang R, Donahue M J and Lomakin V 2016 *IEEE Trans. Magn.* **52**
 [46] Chang R, Li S, Lubarda M V, Livshitz B and Lomakin V 2011 *J. Appl. Phys.* **109** 07D358
 [47] Suess D, Tsiantos V, Schrefl T, Fidler J, Scholz W, Forster H, Dittrich R and Miles J 2002 *J. Magn. Magn. Mater.* **248** 298–311
 [48] Fredkin D R and Koehler T R 1988 *IEEE Trans. Magn.* **24** 2362–7
 [49] Andreas C, Kákay A and Hertel R 2014 *Phys. Rev. B* **89** 134403
 [50] García-Palacios J L and Lázaro F J 1998 *Phys. Rev. B* **58** 14937–58
 [51] d'Aquino M, Serpico C, Coppola G, Mayergoyz I D and Bertotti G 2006 *J. Appl. Phys.* **99** 08B905
 [52] Berkov D V 2002 *IEEE Trans. Magn.* **38** 2489–95
 [53] Zivieri R and Consolo G 2012 *Adv. Condens. Matter Phys.* **2012** 765709
 [54] Krawczyk M and Puzkarski H 2008 *Phys. Rev. B* **77** 054437

- [55] Romero Vivas J, Mamica S, Krawczyk M and Kruglyak V V 2012 *Phys. Rev. B* **86** 144417
- [56] Vansteenkiste A, Leliaert J, Dvornik M, Helsen M, Garcia-Sanchez F and Van Waeyenberge B 2014 *AIP Adv.* **4** 107133
- [57] Kakay A, Westphal E and Hertel R 2010 *IEEE Trans. Magn.* **46** 2303–6
- [58] Zhu R 2016 *AIP Adv.* **6** 056401
- [59] Palmesi P, Exl L, Bruckner F, Abert C and Suess D 2017 *J. Magn. Magn. Mater.* **442** 409–16
- [60] Donahue M J 2009 *IEEE Trans. Magn.* **45** 3923–5
- [61] Choo K, Panlener W and Jang B 2014 Understanding and optimizing GPU cache memory performance for compute workloads *IEEE 13th Int. Symp. on Parallel and Distributed Computing* pp 189–96
- [62] Stratton J A, Anssari N, Rodrigues C, Sung I J, Obeid N, Chang L, Liu G D and Hwu W-m 2012 Optimization and architecture effects on GPU computing workload performance *Innovative Parallel Computing* pp 1–10
- [63] Hestness J, Keckler S W and Wood D A 2015 GPU computing pipeline inefficiencies and optimization opportunities in heterogeneous CPU-GPU processors *IEEE Int. Symp. on Workload Characterization* pp 87–97
- [64] Drews A, Krüger B, Selke G, Kamionka T, Vogel A, Martens M, Merkt U, Möller D and Meier G 2012 *Phys. Rev. B* **85** 144417
- [65] Khan F G, Montrucchio B, Jan B, Khan A N, Jadoon W, Shamshirband S, Chronopoulos A T and Khan I A 2017 *Concurr. Comput.* **29** e3981
- [66] Dvornik M, Vansteenkiste A and Van Waeyenberge B 2014 *Appl. Phys. Lett.* **105** 162411
- [67] Li S, Livshitz B and Lomakin V 2010 *IEEE Trans. Magn.* **46** 2373–5
- [68] Thiele A A 1973 *Phys. Rev. Lett.* **30** 230–3
- [69] Choe S, Acremann Y, Scholl A, Bauer A, Doran A, Stöhr J and Padmore H 2004 *Science* **304** 420–2
- [70] Van Waeyenberge B *et al* 2006 *Nature* **444** 461–4
- [71] Yamada K, Kasai S, Nakatani Y, Kobayashi K, Kohno H, Thiaville A and Ono T 2007 *Nat. Mater.* **6** 269–73
- [72] Dieterle G, Gangwar A, Graefe J, Noske M, Foerster J, Woltersdorf G, Stoll H, Back C H and Schuetz G 2016 *Appl. Phys. Lett.* **108** 022401
- [73] Ding J *et al* 2016 *AIP Adv.* **6** 056102
- [74] Fried J P and Metaxas P J 2017 *IEEE Magn. Lett.* **8**
- [75] Fried J P and Metaxas P J 2016 *Phys. Rev. B* **93** 064422
- [76] Pribiag V S, Krivorotov I N, Fuchs G D, Braganca P M, Ozatay O, Sankey J C, Ralph D C and Buhrman R A 2007 *Nat. Phys.* **3** 498–503
- [77] Perna S, Lopez-Diaz L, d'Aquino M and Serpico C 2016 *Sci. Rep.* **6** 31630
- [78] Kuepferling M, Zullino S, Sola A, Van de Wiele B, Durin G, Pasquale M, Rott K, Reiss G and Bertotti G 2015 *J. Appl. Phys.* **117** 17E107
- [79] Thiaville A, García J M, Dittrich R, Miltat J and Schrefl T 2003 *Phys. Rev. B* **67** 094410
- [80] Noske M, Stoll H, Faehle M, Hertel R and Schuetz G 2015 *Phys. Rev. B* **91** 014414
- [81] Nakatani Y, Hayashi N, Ono T and Miyajima H 2001 *IEEE Trans. Magn.* **37** 2129–31
- [82] Nakatani Y, Thiaville A and Miltat J 2003 *Nat. Mater.* **2** 521–3
- [83] Thiaville A, Garcia J M and Miltat J 2002 *J. Magn. Magn. Mater.* **242–5** 1061–3
- [84] Thiaville A, Nakatani Y, Miltat J and Suzuki Y 2005 *Europhys. Lett.* **69** 990–6
- [85] Mougín A, Cormier M, Adam J P, Metaxas P J and Ferré J 2007 *Europhys. Lett.* **78** 57007
- [86] Nasser S A, Sarma B, Durin G and Serpico C 2015 *Phys. Proc.* **75** 974–85 (20th Int. Conf. on Magnetism)
- [87] Vandermeulen J, Van de Wiele B, Vansteenkiste A, Van Waeyenberge B and Dupré L 2015 *J. Phys. D: Appl. Phys.* **48** 035001
- [88] Vandermeulen J, Nasser S A, Van de Wiele B, Durin G, Van Waeyenberge B and Dupré L 2016 *J. Phys. D: Appl. Phys.* **49** 465003
- [89] Franke K J A, Van de Wiele B, Shirahata Y, Hämäläinen S J, Taniyama T and van Dijken S 2015 *Phys. Rev. X* **5** 011010
- [90] Van de Wiele B, Leliaert J, Franke K J and Van Dijken S 2016 *New J. Phys.* **18** 033027
- [91] López González D, Shirahata Y, Van de Wiele B, Franke K J, Casiraghi A, Taniyama T and van Dijken S 2017 *AIP Adv.* **7** 035119
- [92] Boule O, Malinowski G and Kläui M 2011 *Mater. Sci. Eng. R* **72** 159–87
- [93] Hata H, Taniguchi T, Lee H W, Moriyama T and Ono T 2014 *Appl. Phys. Exp.* **7** 033001
- [94] Sukhov A, Chotorlishvili L, Ernst A, Zubizarreta X, Ostanin S, Mertig I, Gross E K and Berakdar J 2016 *Sci. Rep.* **6** 24411
- [95] Beach G S D, Knutson C, Tsoi M and Erskine J L 2007 *J. Magn. Magn. Mater.* **310** 2038–40
- [96] Nakatani Y, Thiaville A and Miltat J 2005 *J. Magn. Magn. Mater.* **290–291** 750–3
- [97] Estévez V and Laurson L 2015 *Phys. Rev. B* **91** 054407
- [98] Estévez V and Laurson L 2016 *Phys. Rev. B* **93** 064403
- [99] Estévez V and Laurson L 2017 *Phys. Rev. B* **96** 064420
- [100] Kläui M *et al* 2006 *Appl. Phys. Lett.* **88** 232507
- [101] Thiaville A, Rohart S, Jué É, Cros V and Fert A 2012 *Europhys. Lett.* **100** 57002
- [102] Benitez M, Hrabec A, Mihai A, Moore T, Burnell G, McGrouther D, Marrows C and McVitie S 2015 *Nat. Commun.* **6** 8957
- [103] Stein F U, Bocklage L, Weigand M and Meier G 2014 *Phys. Rev. B* **89** 024423
- [104] Thiaville A and Nakatani Y 2006 Domain-wall dynamics in nanowires and nanostrips *Spin Dynamics in Confined Magnetic Structures III (Topics in Applied Physics)* vol 101 (Berlin: Springer) pp 161–205
- [105] Clarke D J, Tretiakov O A, Chern G W, Bazaliy Y B and Tchernyshyov O 2008 *Phys. Rev. B* **78** 134412
- [106] Leliaert J, Van de Wiele B, Vansteenkiste A, Laurson L, Durin G, Dupré L and Van Waeyenberge B 2014 *Phys. Rev. B* **89** 064419
- [107] Sanchez-Tejerina L, Alejos O, Martinez E and Munoz J M 2016 *J. Magn. Magn. Mater.* **409** 155–62
- [108] Martinez E, Alejos O, Auxiliadora Hernandez M, Raposo V, Sanchez-Tejerina L and Moretti S 2016 *Appl. Phys. Exp.* **9** 063008
- [109] Herranen T and Laurson L 2015 *Phys. Rev. B* **92** 100405
- [110] Brataas A and Hals K M D 2014 *Nat. Nanotechnol.* **9** 86–8
- [111] Khvalkovskiy A V, Cros V, Apalkov D, Nikitin V, Krounbi M, Zvezdin K A, Anane A, Grollier J and Fert A 2013 *Phys. Rev. B* **87** 020402
- [112] Martinez E, Finocchio G, Torres L and Lopez-Diaz L 2013 *AIP Adv.* **3** 072109
- [113] Boule O, Buda-Prejbeanu L D, Jué E, Miron I M and Gaudin G 2014 *J. Appl. Phys.* **115** 17D502
- [114] Martinez E 2012 *J. Phys.: Condens. Matter* **24** 024206
- [115] Martinez E 2012 *J. Magn. Magn. Mater.* **324** 3542–7
- [116] Van de Wiele B, Laurson L and Durin G 2012 *Phys. Rev. B* **86** 144415
- [117] Kim J S *et al* 2010 *Phys. Rev. B* **82** 104427
- [118] Burgess J A J, Fraser A E, Fani Sani F, Vick D, Hauer B D, Davis J P and Freeman M R 2013 *Science* **339** 1051–4
- [119] Chen T Y, Erickson M J, Crowell P A and Leighton C 2012 *Phys. Rev. Lett.* **109** 097202
- [120] Miltat J and Thiaville A 2002 *Science* **298** 555
- [121] Leliaert J, Van de Wiele B, Vansteenkiste A, Laurson L, Durin G, Dupré L and Van Waeyenberge B 2014 *J. Appl. Phys.* **115** 17D102
- [122] Lau J, McMichael R and Donahue M 2009 *J. Res. Natl Inst. Stand. Technol.* **114** 5767

- [123] Leliaert J, Van de Wiele B, Vansteenkiste A, Laurson L, Durin G, Dupré L and Van Waeyenberge B 2014 *J. Appl. Phys.* **115** 233903
- [124] Min H, McMichael R D, Donahue M J, Miltat J and Stiles M D 2010 *Phys. Rev. Lett.* **104** 217201
- [125] Voto M, Lopez-Diaz L, Torres L and Moretti S 2016 *Phys. Rev. B* **94** 174438
- [126] Tserkovnyak Y, Skadsem H J, Brataas A and Bauer G E W 2006 *Phys. Rev. B* **74** 144405
- [127] Berkov D and Miltat J 2008 *J. Magn. Magn. Mater.* **320** 1238–59
- [128] Ban Y and Tataru G 2009 *Phys. Rev. B* **80** 184406
- [129] Kläui M *et al* 2005 *Phys. Rev. Lett.* **95** 026601
- [130] Heyne L *et al* 2008 *Phys. Rev. Lett.* **100** 066603
- [131] Lepadatu S, Vanhaverbeke A, Atkinson D, Allenspach R and Marrows C H 2009 *Phys. Rev. Lett.* **102** 127203
- [132] Lepadatu S, Hickey M C, Potenza A, Marchetto H, Charlton T R, Langridge S, Dhessi S S and Marrows C H 2009 *Phys. Rev. B* **79** 094402
- [133] Lepadatu S *et al* 2010 *Phys. Rev. B* **81** 020413
- [134] Eltschka M *et al* 2010 *Phys. Rev. Lett.* **105** 056601
- [135] Thomas L, Hayashi M, Jiang X, Moriya R, Rettner C and Parkin S P 2006 *Nature* **443** 197–200
- [136] Heyne L *et al* 2010 *Phys. Rev. Lett.* **105** 187203
- [137] Pollard S D, Huang L, Buchanan K S, Arena D A and Zhu Y 2012 *Nat. Commun.* **3** 1028
- [138] Meier G, Bolte M, Eiselt R, Krüger B, Kim D H and Fischer P 2007 *Phys. Rev. Lett.* **98** 187202
- [139] Hayashi M, Thomas L, Bazaliy Y B, Rettner C, Moriya R, Jiang X and Parkin S P 2006 *Phys. Rev. Lett.* **96** 197207
- [140] Beach G S D, Knutson C, Nistor C, Tsoi M and Erskine J L 2006 *Phys. Rev. Lett.* **97** 057203
- [141] Heyne L, Rhensius J, Bisig A, Krzyk S, Punke P, Kläui M, Heyderman L J, Guyader L L and Nolting F 2010 *Appl. Phys. Lett.* **96** 032504
- [142] Martinez E, Lopez-Diaz L, Torres L, Tristan C and Alejos O 2007 *Phys. Rev. B* **75** 174409
- [143] Leliaert J, Van de Wiele B, Vandermeulen J, Coene A, Vansteenkiste A, Laurson L, Durin G, Van Waeyenberge B and Dupré L 2015 *Appl. Phys. Lett.* **106** 202401
- [144] Hayward T J 2015 *Sci. Rep.* **5** 13279
- [145] Kim J, Je S G and Choe S B 2015 *Appl. Phys. Exp.* **8** 063001
- [146] Metaxas P J, Jamet J P, Mougou A, Cormier M, Ferré J, Baltz V, Rodmacq B, Dieny B and Stamps R L 2007 *Phys. Rev. Lett.* **99** 217208
- [147] Lemerle S, Ferré J, Chappert C, Mathet V, Giamarchi T and Le Doussal P 1998 *Phys. Rev. Lett.* **80** 849–52
- [148] Chauve P, Giamarchi T and Le Doussal P 2000 *Phys. Rev. B* **62** 6241–67
- [149] Kim K J, Lee J C, Ahn S M, Lee K S, Lee C W, Cho Y J, Seo S, Shin K H, Choe S B and Lee H W 2009 *Nature* **458** 740–2
- [150] Leliaert J, Van de Wiele B, Vansteenkiste A, Laurson L, Durin G, Dupré L and Van Waeyenberge B 2016 *Sci. Rep.* **6** 20472
- [151] Hayward T and Omari K 2017 *J. Phys. D: Appl. Phys.* **50** 084006
- [152] Moretti S, Voto M and Martinez E 2017 *Phys. Rev. B* **96** 054433
- [153] Herranen T and Laurson L 2017 *Phys. Rev. B* **96** 144422
- [154] Zverev V V and Filippov B N 2016 *Phys. Solid State* **58** 485–96
- [155] Zverev V, Filippov B and Dubovik M 2017 *Phys. Solid State* **59** 520–31
- [156] Novotechnik 2015 *White Pap.* (<http://www.novotechnik.com/news/Resources/MultiturnWhitePaperV4.pdf>)
- [157] Parkin S and Yang S H 2015 *Nat. Nanotechnol.* **10** 195–8
- [158] Parkin S, Hayashi M and Thomas L 2008 *Science* **320** 190–4
- [159] Hayashi M, Thomas L, Moriya R, Rettner C and Parkin S P 2008 *Science* **320** 209–11
- [160] Purnama I, Murapaka C S, Lew W S and Ono T 2014 *Appl. Phys. Lett.* **104** 092414
- [161] Kläui M, Vaz C A F, Bland J A C, Wernsdorfer W, Faini G, Cambil E, Heyderman L J, Nolting F and Rudiger U 2005 *Phys. Rev. Lett.* **94** 106601
- [162] Yuan H and Wang X 2015 *Phys. Rev. B* **92** 054419
- [163] Zhou X, Huang Z, Zhang W, Yin Y, Dürrenfeld P, Dong S and Zhai Y 2017 *AIP Adv.* **7** 056014
- [164] Chiba D *et al* 2010 *Appl. Phys. Exp.* **3** 073004
- [165] Tomasello R, Martinez E, Zivieri R, Torres L, Carpentieri M and Finocchio G 2014 *Sci. Rep.* **4** 06784
- [166] Yang L *et al* 2015 *Sci. Rep.* **5** 16942
- [167] Sánchez-Tejerina L, Alejos Ó, Martínez E and Raposo V 2017 arXiv:1705.00905
- [168] Allwood D A, Xiong G, Faulkner C C, Atkinson D, Petit D and Cowburn R P 2005 *Science* **309** 16881692
- [169] Atkinson D, Faulkner C C, Allwood D A and Cowburn R 2006 Chapter: Domain-wall dynamics in magnetic logic devices *Spin Dynamics in Confined Magnetic Structures III (Topics in Applied Physics vol 101)* (Berlin: Springer) pp 207–23
- [170] Barnes S E, Ieda J and Maekawa S 2006 *Appl. Phys. Lett.* **89** 122507
- [171] Omari K A and Hayward T J 2014 *Phys. Rev. Appl.* **2** 044001
- [172] Goolaup S, Ramu M, Murapaka C and Lew W 2015 *Sci. Rep.* **5** 9603
- [173] Bisig A *et al* 2015 *Appl. Phys. Lett.* **106** 122401
- [174] Omari K, Bradley R C, Broomhall T J, Hodges M P P, Rosamond M C, Linfield E H, Im M Y, Fischer P and Hayward T J 2015 *Appl. Phys. Lett.* **107** 222403
- [175] Vandermeulen J, Van de Wiele B, Dupré L and Van Waeyenberge B 2015 *J. Phys. D: Appl. Phys.* **48** 275003
- [176] Gonzalez D L, Casiraghi A, Van de Wiele B and van Dijken S 2016 *Appl. Phys. Lett.* **108** 032402
- [177] Rohart S, Miltat J and Thiaville A 2016 *Phys. Rev. B* **93** 214412
- [178] Fert A, Reyren N and Cros V 2017 *Nat. Rev. Mater.* **2** 17031
- [179] Rohart S and Thiaville A 2013 *Phys. Rev. B* **88** 184422
- [180] Bessarab P F, Uzdin V M and Jönsson H 2015 *Comput. Phys. Commun.* **196** 335–47
- [181] Lobanov I S, Jönsson H and Uzdin V M 2016 *Phys. Rev. B* **94** 174418
- [182] Cortes-Ortuno D *et al* 2017 *Sci. Rep.* **7** 4060
- [183] Stosic D, Mulkers J, Van Waeyenberge B, Ludermir T and Milošević M V 2017 *Phys. Rev. B* **95** 214418
- [184] Chui C P, Ma F and Zhou Y 2015 *AIP Adv.* **5** 047141
- [185] Mulkers J, Milošević M V and Van Waeyenberge B 2016 *Phys. Rev. B* **93** 214405
- [186] Exl L, Bance S, Reichel F, Schrefl T, Peter Stimming H and Mauser N J 2014 *J. Appl. Phys.* **115** 17D118
- [187] Woo S *et al* 2016 *Nat. Mater.* **15** 501–6
- [188] Sampaio J, Cros V, Rohart S, Thiaville A and Fert A 2013 *Nat. Nanotech.* **8** 839–44
- [189] Rosch A 2013 *Nature* **8** 160–1
- [190] Tomasello R, Martinez E, Zivieri R, Torres L, Carpentieri M and Finocchio G 2014 *Sci. Rep.* **4** 6784
- [191] Iwasaki J, Mochizuki M and Nagaosa N 2013 *Nat. Nanotech.* **8** 742–7
- [192] Kim J and Yoo M 2017 *Appl. Phys. Lett.* **110** 132404
- [193] Zhang X, Zhou Y, Ezawa M, Zhao G P and Zhao W 2015 *Sci. Rep.* **5** 11369
- [194] Mulkers J, Van Waeyenberge B and Milošević M V 2017 *Phys. Rev. B* **95** 144401
- [195] Udvardi L and Szunyogh L 2009 *Phys. Rev. Lett.* **102** 1–4
- [196] Kruglyak V V, Demokritov S O and Grundler D 2010 *J. Phys. D: Appl. Phys.* **43** 264001

- [197] Au Y, Dvornik M, Davison T, Ahmad E, Keatley P S, Vansteenkiste A, Van Waeyenberge B and Kruglyak V 2013 *Phys. Rev. Lett.* **110** 097201
- [198] Fazlali M, Dvornik M, Iacocca E, Durrenfeld P, Haidar M, Åkerman J and Dumas R K 2016 *Phys. Rev. B* **93** 134427
- [199] Van de Wiele B, Hamalainen S J, Balaz P, Montoncello F and van Dijken S 2016 *Sci. Rep.* **6** 21330
- [200] Demidov V E, Urazhdin S, Liu R, Divinskiy B, Telegin A and Demokritov S O 2016 *Nat. Commun.* **7** 10446
- [201] Klingler S, Pirro P, Braecher T, Leven B, Hillebrands B and Chumak A V 2015 *Appl. Phys. Lett.* **106** 212406
- [202] Gruszecki P, Romero-Vivas J, Dadoenkova Y S, Dadoenkova N N, Lyubchanskii I L and Krawczyk M 2014 *Appl. Phys. Lett.* **105** 242406
- [203] Stigloher J *et al* 2016 *Phys. Rev. Lett.* **117** 037204
- [204] Garcia-Sanchez F, Borys P, Soucaille R, Adam J P, Stamps R L and Kim J 2015 *Phys. Rev. Lett.* **114** 247206
- [205] Wagner K, Kakay A, Schultheiss K, Henschke A, Sebastian T and Schultheiss H 2016 *Nat. Nanotech.* **11** 432–6
- [206] Borys P, Garcia-Sanchez F, Kim J and Stamps R L 2016 *Adv. Electron. Mater.* **2** 1500202
- [207] Helsen M, Gangwar A, De Clercq J, Vansteenkiste A, Weigand M, Back C H and Van Waeyenberge B 2015 *Appl. Phys. Lett.* **106** 032405
- [208] Bauer H G, Majchrak P, Kachel T, Back C H and Woltersdorf G 2015 *Nat. Commun.* **6** 8274
- [209] Metaxas P J *et al* 2015 *Appl. Phys. Lett.* **106** 232406
- [210] Sushruth M *et al* 2016 *Phys. Rev. Appl.* **6** 044005
- [211] Houshang A, Iacocca E, Durrenfeld P, Sani S R, Åkerman J and Dumas R K 2016 *Nat. Nanotech.* **11** 280–6
- [212] Awad A A, Durrenfeld P, Houshang A, Dvornik M, Iacocca E, Dumas R K and Åkerman J 2017 *Nat. Phys.* **13** 292–9
- [213] Dvornik M, Awad A A and Åkerman J 2017 arXiv:1702.04155
- [214] Flovik V, Macia F and Wahlstrom E 2016 *Sci. Rep.* **6** 32528
- [215] Demidov V, Urazhdin S, Zholud A, Sadovnikov A, Slavin A and Demokritov S 2015 *Sci. Rep.* **5** 8578
- [216] Iacocca E, Durrenfeld P, Heinonen O, Åkerman J and Dumas R K 2015 *Phys. Rev. B* **91** 104405
- [217] Bonetti S *et al* 2015 *Nat. Commun.* **6** 8889
- [218] Jungfleisch M B *et al* 2016 *Phys. Rev. Lett.* **116** 057601
- [219] Durrenfeld P, Awad A A, Houshang A, Dumas R K and Åkerman J 2017 *Nanoscale* **9** 1285–91
- [220] Iacocca E, Dumas R K, Bookman L, Mohseni M, Chung S, Hofer M A and Åkerman J 2014 *Phys. Rev. Lett.* **112** 047201
- [221] Lendínez S, Statuto N, Backes D, Kent A D and Macià F 2015 *Phys. Rev. B* **92** 174426
- [222] Wills P, Iacocca E and Hofer M A 2016 *Phys. Rev. B* **93** 144408
- [223] Xiao D, Liu Y, Zhou Y, Mohseni S M, Chung S and Åkerman J 2016 *Phys. Rev. B* **93** 094431
- [224] Wang C, Xiao D, Zhou Y, Åkerman J and Liu Y 2017 *AIP Adv.* **7** 056019
- [225] Loreto R, Moura-Melo W, Pereira A, Zhang X, Zhou Y, Ezawa M and de Araujo C 2017 *J. Magn. Magn. Mater.* at press
- [226] Zhou Y, Iacocca E, Awad A, Dumas R, Zhang F, Braun H and Åkerman J 2015 *Nat. Commun.* **6** 8193
- [227] Garcia-Sanchez F, Sampaio J, Reyren N, Cros V and Kim J V 2016 *New. J. Phys.* **18** 075011
- [228] Durrenfeld P, Xu Y, Åkerman J and Zhou Y 2017 *Phys. Rev. B* **96** 054430
- [229] Arai K *et al* 2012 *Phys. Rev. B* **85** 104418
- [230] Radu F, Zabel H and Bader S D 2008 *Exchange Bias Effect of Ferro-/Antiferromagnetic Heterostructures* (Berlin: Springer) pp 97–184
- [231] Folven E, Scholl A, Young A, Retterer S T, Boschker J E, Tybell T, Takamura Y and Grepstad J K 2012 *Nano lett.* **12** 2386–90
- [232] Moran T J, Nogus J, Lederman D and Schuller I K 1998 *Appl. Phys. Lett.* **72** 617–9
- [233] Schulthess T C and Butler W H 1998 *Phys. Rev. Lett.* **81** 4516–9
- [234] De Clercq J, Leliaert J and Van Waeyenberge B 2017 *J. Phys. D: Appl. Phys.* **50** 425002
- [235] Skumryev V, Stoyanov S, Zhang Y, Hadjipanayis G, Givord D and Nogués J 2003 *Nature* **423** 850–3
- [236] Folven E *et al* 2015 *Phys. Rev. B* **92** 094421
- [237] Fukami S, Zhang C, DuttaGupta S, Kurenkov A and Ohno H 2016 *Nat. Mater.* **15** 535–41
- [238] You L, Lee O, Bhowmik D, Labanowski D, Hong J, Bokor J and Salahuddin S 2015 *Proc. Natl Acad. Sci. USA* **112** 10310–5
- [239] Liu L, Lee O J, Gudmundsen T J, Ralph D C and Buhrman R A 2012 *Phys. Rev. Lett.* **109** 096602
- [240] Mauri D, Siegmann H C, Bagus P S and Kay E 1987 *J. Appl. Phys.* **62** 3047–9
- [241] Kiwi M 2001 *J. Magn. Magn. Mater.* **234** 584–95
- [242] Evans R F, Fan W J, Chureemart P, Ostler T A, Ellis M O and Chantrell R W 2014 *J. Phys.: Condens. Matter* **26** 103202
- [243] De Clercq J, Vansteenkiste A, Abes M, Temst K and Van Waeyenberge B 2016 *J. Phys. D: Appl. Phys.* **49** 435001
- [244] Dias T, Menéndez E, Liu H, Van Haesendonck C, Vantomme A, Temst K, Schmidt J E, Giulian R and Geshev J 2014 *J. Appl. Phys.* **115** 243903
- [245] Brems S, Volodin A, Haesendonck C V and Temst K 2008 *J. Appl. Phys.* **103** 113912
- [246] Brems S, Buntinx D, Temst K, Van Haesendonck C, Radu F and Zabel H 2005 *Phys. Rev. Lett.* **95** 157202
- [247] Radu F, Eitzkorn M, Siebrecht R, Schmitte T, Westerholt K and Zabel H 2003 *Phys. Rev. B* **67** 134409
- [248] Kiwi M, Mejiá-López J, Portugal R and Ramirez R 2000 *Solid State Commun.* **116** 315–9
- [249] Phuoc N N, Thuy N P, Tuan N A, Hung L T, Thanh N T and Nam N T 2006 *J. Magn. Magn. Mater.* **298** 43–7
- [250] Petravic O, Li Z P, Roshchin I V, Viret M, Morales R, Batlle X and Schuller I K 2005 *Appl. Phys. Lett.* **87** 222509
- [251] Leighton C, Nogués J, Jönsson-Åkerman B and Schuller I K 2000 *Phys. Rev. Lett.* **84** 3466
- [252] Takamura Y *et al* 2013 *Phys. Rev. Lett.* **111** 107201
- [253] Hoffmann A 2004 *Phys. Rev. Lett.* **93** 097203
- [254] Farhan A, Derlet P, Kleibert A, Balan A, Chopdekar R, Wyss M, Anghinolfi L, Nolting F and Heyderman L 2013 *Nat. Phys.* **9** 375
- [255] Ramirez A P, Hayashi A, Cava R, Siddharthan R and Shastry B 1999 *Nature* **399** 333–5
- [256] Nisoli C, Moessner R and Schiffer P 2013 *Rev. Mod. Phys.* **85** 1473–90
- [257] Wang R *et al* 2006 *Nature* **439** 303–6
- [258] Budrikis Z, Politi P and Stamps R L 2012 *New. J. Phys.* **14** 045008
- [259] Morgan J, Stein A, Langridge S and Marrows C 2011 *New. J. Phys.* **13** 105002
- [260] Chern G W, Reichhardt C and Reichhardt C O 2014 *New. J. Phys.* **16** 063051
- [261] Reichhardt C J O, Chern G W, Libl A and Reichhardt C 2015 *J. Appl. Phys.* **117** 172612

- [262] Porro J M, Bedoya-Pinto A, Berger A and Vavassori P 2013 *New J. Phys.* **15** 055012
- [263] Kapaklis V, Arnalds U B, Farhan A, Chopdekar R V, Balan A, Scholl A, Heyderman L J and Hjörvarsson B 2014 *Nat. Nanotechnol.* **9** 514–9
- [264] Van de Wiele B, Fin S, Pancaldi M, Vavassori P, Sarella A and Bisero D 2016 *J. Appl. Phys.* **119** 203901
- [265] Li Y *et al* 2017 *J. Phys. D: Appl. Phys.* **50** 015003
- [266] Tanaka M, Saitoh E, Miyajima H, Yamaoka T and Iye Y 2006 *Phys. Rev. B* **73** 052411
- [267] Ladak S, Read D, Perkins G, Cohen L and Branford W 2010 *Nat. Phys.* **6** 359–63
- [268] Tchernyshyov O 2010 *Nat. Phys.* **6** 323–4
- [269] Daunheimer S A, Petrova O, Tchernyshyov O and Cumings J 2011 *Phys. Rev. Lett.* **107** 167201
- [270] Pushp A, Phung T, Rettner C, Hughes B P, Yang S H, Thomas L and Parkin S S 2013 *Nat. Phys.* **9** 505–11
- [271] Krishnia S, Purnama I and Lew W S 2016 *J. Magn. Magn. Mater.* **420** 158–65
- [272] Park J, Le B L, Sklenar J, Chern G W, Watts J D and Schiffer P 2017 *Phys. Rev. B* **96** 024436
- [273] Shen Y, Petrova O, Mellado P, Daunheimer S, Cumings J and Tchernyshyov O 2012 *New J. Phys.* **14** 035022
- [274] Dvornik M, Vansteenkiste A and Van Waeyenberge B 2013 *Phys. Rev. B* **88** 054427
- [275] Nembach H T, Shaw J M, Boone C T and Silva T J 2013 *Phys. Rev. Lett.* **110** 117201
- [276] Weindler T, Bauer H G, Islinger R, Boehm B, Chauleau J Y and Back C H 2014 *Phys. Rev. Lett.* **113** 237204
- [277] Wang W *et al* 2015 *Phys. Rev. B* **92** 054430